Lifelong and Universal Machine Learning Potentials for Chemical Reaction Network Explorations

Marco Eckhoff* and Markus Reiher†
ETH Zurich, Department of Chemistry and Applied Biosciences, Vladimir-Prelog-Weg 2, 8093 Zurich, Switzerland.
(Dated: April 16, 2025)

Recent developments in computational chemistry facilitate the automated quantum chemical exploration of chemical reaction networks for the in-silico prediction of synthesis pathways, yield, and selectivity. However, the underlying quantum chemical energy calculations require vast computational resources, limiting these explorations severely in practice. Machine learning potentials (MLPs) offer a solution to increase computational efficiency, while retaining the accuracy of reliable first-principles data used for their training. Unfortunately, MLPs will be limited in their generalization ability within chemical (reaction) space, if the underlying training data is not representative for a given application. Within the framework of automated reaction network exploration, where new reactants or reagents composed of any elements from the periodic table can be introduced, this lack of generalizability will be the rule rather than the exception. Here, we therefore study the benefits and drawbacks of two MLP concepts in this context. Whereas universal MLPs are designed to cover most of the relevant chemical space in their training, lifelong MLPs push their adaptability by efficient continual learning of additional data. While the accuracy of the universal MLPs turns out to be not yet sufficient for reaction search trials without any fine-tuning, lifelong MLPs can reach chemical accuracy. We propose an improved learning algorithm for lifelong adaptive data selection yielding efficient integration of new data while previous expertise is preserved.

Keywords: Lifelong Machine Learning Potentials, Universal Machine Learning Potentials, Chemical Reaction Networks, Continual Resilient (CoRe) Optimizer, Lifelong Adaptive Data Selection

arXiv:2504.11933v1 [physics.chem-ph] 16 Apr 2025

1. INTRODUCTION

In-silico prediction of chemical processes including yield and selectivity can be a key to improving the efficiency of chemical processes and their sustainability [1–3]. However, the reliable representation of reaction kinetics requires knowledge about all possible reactive events. Consequently, large networks of reactions emerge for almost all relevant chemical processes.

The exploration of chemical reaction networks (CRNs) with quantum chemical methods therefore causes immense computational costs in order to identify thousands of stable intermediates and their connecting transition state structures [4–14], which are stationary points on a Born-Oppenheimer potential energy surface. Search trials across this surface can be performed either by explicit construction of potentially reactive complexes [15–23] or through molecular dynamics driven searches [24–29]. However, both approaches require an enormous number of first-principles single-point calculations, which is a challenge that is also persistent in other tasks of computational chemistry, biology, and materials science such as virtual high-throughput screening [30, 31].

Accordingly, fast quantum chemical approaches are needed. However, they are plagued by drastic approximations that compromise not only energies but also molecular structures [32, 33]. As a consequence, a CRN constructed with an approximate quantum chemical approach (such as tight-binding density functional or semi-empirical theories) does not necessarily represent the network that would be obtained with a more reliable approach (such as density functional theory (DFT)). Hence, node and connection fidelity can be compromised. Local refinement by applying more accurate methods for the a-posteriori reoptimization of stable intermediates and transition states could improve molecular structures and, most importantly, their relative energies [34–36]. However, this requires a CRN to be qualitatively correct. Hence, the stationary points optimized with a fast approach must be complete as must be their connections by elementary reaction steps. It is therefore key to devise first-principles-based methods that are (I) fast to allow for efficient reactive event screening and that have (II) high structural fidelity so that the topology and structure of a CRN is not compromised. Hence, machine learning potentials (MLPs) hold the greatest promise to yield both, efficiency and structure fidelity [37–43].

However, the requirements for MLPs in CRN exploration are challenging. (1) They must be quickly initializable and (2) they must not come with an unbearable overhead for their training. It is precisely the the goal of universal MLPs (uMLPs) to deliver a parametrization that is as general as possible to overcome the initialization issue and to avoid training at runtime [44–46]. Unfortunately, an approach without further fine-tuning on some given chemical system can suffer from insufficient accuracy. In order to tackle this challenge, we therefore proposed the concept of lifelong machine learning potentials (lMLP) to alleviate the overhead of training [47].

* eckhoffm@ethz.ch
† mreiher@ethz.ch

In contrast to conventionally trained MLPs, lMLPs can continuously adapt to additional data without forgetting previous knowledge, while they do not require training again on all previous data. Hence, they can offer high accuracy for some parts of chemical space studied, but they may still require additional quantum chemical calculations during their application.

In this work, we assess the reliability, accuracy, and efficiency of both, uMLPs and lMLPs, for CRN explorations. Section 2 summarizes the concepts of lMLPs and uMLPs and introduces an improved algorithm for lifelong adaptive data selection. The computational details are compiled in Section 3. Section 4 starts with a presentation of the HCN+H_2O CRN studied in this work. The section continues with a performance assessment of uMLPs compared to DFT reference data. Afterwards, continual learning of an lMLP on the CRN data is analyzed and compared to conventional iterative learning as well as to uMLP and DFT results.

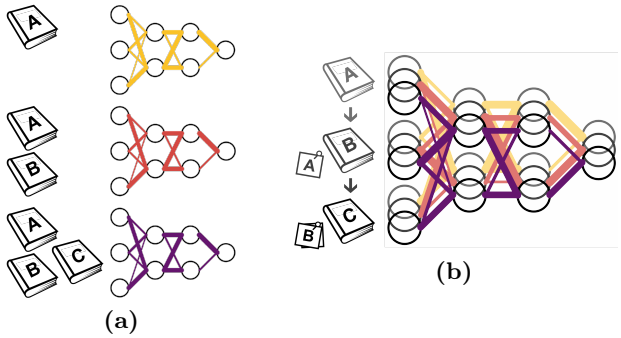

Figure 1: (a) In iterative learning, a new machine learning model is trained from scratch on all data to integrate additional training data. **(a)** In lifelong learning, the training of a model is continued employing added data and only a subset of previous data to prevent forgetting. In this way, previously acquired knowledge of the model is exploited. We note that lifelong learning is here only based on rehearsal of data, while it can also exploit model parameter regularization and model architecture.

2. METHODS

2.1. Lifelong Machine Learning Potentials

The concept of lMLPs [47] introduces continual or lifelong machine learning [48, 49] into the MLP training process. An efficient online learning process can greatly advance the adaptability of MLPs to yield high accuracy and general applicability for every chemical structure within a reasonable period of time. Consequently, lMLPs may require some reference calculations on-the-fly during their application in simulations, but these additional training data can be integrated with low cost. However, continual machine learning is a challenge in itself [50, 51], especially in the single incremental task scenario [52] which is given for the prediction of the potential energy surface for more and more chemical structures. We note that an alternative approach for on-the-fly learning of MLPs can be obtained by Bayesian inference [53, 54].

In conventional iterative learning, each extension of the reference data requires training from scratch on all data to obtain an improved machine learning model. For example, to obtain a model that cannot only represent data A but also data B, a new model (red model in Figure 1) is trained on both data sets simultaneously (Figure 1 (a)). Further extension to data C (purple model in Figure 1) then requires training on all data A+B+C. Consequently, the effort for model adaptions by the same amount of added data increases more and more for larger training data sets. If the training of the previous model was continued only on the added data, so-called catastrophic forgetting would occur, i.e., the previous knowledge vanishes due to the optimization of the model parameters only on new data.

Therefore, continual learning introduces training strategies to mitigate catastrophic forgetting by rehearsal of essential training data, regularization of model parameters, and/or the model architecture. For example, training of a model based on data A (yellow model in Figure 1) can be continued by learning the added data B and a small subset of the previous data A (Figure 1 (b)). This subset only needs to ensure that the already existing knowledge will be retained, i.e., previously acquired knowledge will be exploited and the training cost is reduced. It can be chosen during the previous training process applying, for example, lifelong adaptive data selection (lADS) [47] (see Section 2.4). Subsequently, the learning process can be further continued by training on added data C and a subset of A+B. In this incremental learning approach, training on additional data can be efficient even for large data sets because training again on the entire data set A+B+C can be avoided. Moreover, several continual learning strategies can be combined. For example, the model parameter regularization of the continual resilient (CoRe) optimizer [47, 55] can be applied in addition to lADS.

With the help of continual learning, a closed and efficient loop in the evolution and application of an lMLP can be obtained (Figure 2). The process starts with some initial reference data. These data can be represented through universal descriptors such as element-embracing atom-centered symmetry functions (eeACSFs) [47], so that they can be learned by an lMLP utilizing, for example, the high-dimensional neural network potential (HDNNP) method [56–58] (see Supporting Information Section S1.1 of this work for an overview). We note that the lMLP concept can also be employed with other methods, including approaches which combine descriptor and potential into a single learnable representation. In any case, the representation must be able to handle any chemical structure to yield a generally applicable lMLP.

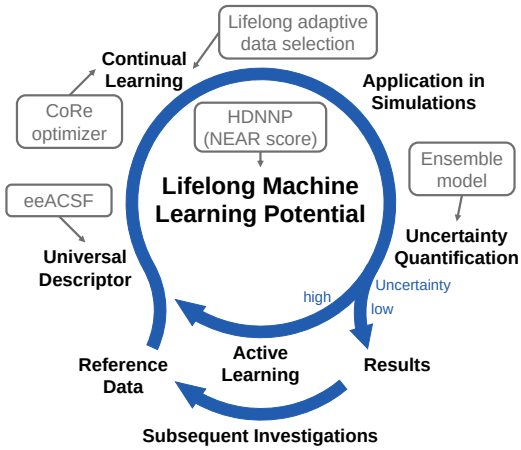

Figure 2: Key conceptual elements of lMLPs denoted in black font. Example methods are denoted in gray (see main text for details). Reference data need to be represented by a universal descriptor to be learned by the lMLP. If simulations encounter lMLP predictions of high uncertainty, active learning tackles this issue in the framework of a continual learning approach for an efficient adaption of the lMLP. Moreover, results obtained in such simulations may point to follow-up simulations, e.g., on related systems, which may then require training on additional data coming in. Data points integrated by continual learning neither require training from scratch, nor on all data.

For example, many MLP descriptors cannot efficiently represent a system with many different chemical elements because their descriptor vector size increases with an increasing number of different elements. As a consequence, the application of conventional atom-centered symmetry functions [59] is often restricted to systems with at most four different elements because of computational costs. By combination of (molecular) structure information with element information of the periodic table, eeACSFs can overcome this limitation [47, 60] (see Supporting Information Section S1.2 of this work for an overview). Moreover, in Supporting Information Section S1.2 of this work we propose alternative functions based on the bump function to represent the radial and angular structure within eeACSFs and we introduce the cube root-scaled-shifted (crss) scaling function for eeACSFs.

To be able to deal with molecules with different total charges or spin multiplicities, individual lMLPs for each state can be trained. Alternatively, the second-generation HDNNP base model can be replaced by other models that can handle multiple states, such as fourth-generation HDNNPs [61]. Moreover, continual learning can also be applied to train atomic-property machine learning models (e.g., for atomic charges and spins) to calculate these efficiently, e.g., during molecular dynamics simulations.

The trained model can subsequently be applied, whereby uncertainty quantification can be exploited to probe a pre-defined accuracy on the fly and to identify the need for new data points. In fact, uncertainty quantification is necessary to enable application of an lMLP at every training stage because it provides the confidence interval for analysis of the results. Uncertainties can be obtained, for example, by an ensemble or committee model [62–65]. This can provide a quantitative estimate of small errors, while large errors can only be flagged. However, an indication of large errors is sufficient because only the need for additional data must be revealed. Those are then produced and fed into the continual training process until all errors are found to be sufficiently small.

In case of high uncertainties, active learning with a query-by-committee approach can be applied to complete the training data sampling. In active learning of MLPs, (I) missing training data are identified during MLP application based on the uncertainty assessed, (II) uncertainly predicted chemical structures are recalculated by the reference method, and (III) the MLP is retrained. Continual learning can be applied to speed up the retraining process compared to the conventional application of iterative learning during active learning. Hence, lifelong learning and active learning therefore complement one another. In addition, chemical insights resulting from the simulations may lead to subsequent tasks, which require reference data of further chemical systems or reactions. These can be generated by various approaches in order to extend the model (such as (random) variations of experimental or handcrafted structures or ab initio molecular dynamics simulations). Also here, continual learning can fasten the adaption of the model to these data.

Therefore, we note that lifelong or continual learning can be a sub-task of active learning, but generally speaking it refers to a continual model (re-)training process and can be applied without training data generation by active learning. Continual learning itself does not include a training data generation workflow in contrast to active learning. It allows us to avoid inefficient model training on all previous training data from scratch again.

2.2. Lifelong Adaptive Data Selection

Lifelong adaptive data selection (lADS) is a continual learning algorithm utilizing rehearsal of previous training data. Its goal is a continuous reduction of the training data to distill important data for (re-)training in continual learning. Moreover, it includes a mechanism to remove inconsistent data, which is necessary in online learning due to limited options for data pre-processing. In addition, lADS ranks the data points according to their importance for training to improve learning efficiency.

The main ideas behind lADS are that, on the one hand, training data will be redundant if they are seldom trained in continual learning but still well represented. On the other hand, it is likely that data will be inconsistent with the majority of data if they are very often trained but still

poorly represented. Consequently, lADS requires only a fraction of all training structures in each training step, applying a biased random selection. The probability for training of a given structure thereby needs to be adjusted according to how well the structure is represented by the model and how stable the quality of this representation is. In this way, both aforementioned ideas can be exploited. Moreover, learning can also focus on the insufficiently represented training data.

To determine whether a structure is well or poorly represented, the loss is utilized. The loss is the property that is minimized during training, representing the difference between model predictions and reference values. The total loss is a sum of the contributions of all N_{fit} structures r,

$$L_{\mathrm{total}} = \sum_{r=1}^{N_{\mathrm{fit}}} \frac{q}{N_{\mathrm{fit}}} \mathcal{L}\left(\frac{E^r}{N_{\mathrm{atom}}^r}\right) + \frac{\mathcal{L}\left(\mathbf{F}^r\right)}{3N_{\mathrm{atom}}^{\mathrm{fit,sum}}} \ , \qquad (1)$$

with the loss functions $\mathcal{L}$ of the energy E^r and atomic force components $F_{\alpha,n}^r$ of the N_{atom}^r atoms n of each structure r,

$$\mathcal{L}\left(\frac{E^r}{N_{\mathrm{atom}}^r}\right) = \left(\frac{E^r - E^{\mathrm{ref},r}}{N_{\mathrm{atom}}^r}\right)^2 \ , \qquad (2)$$

$$\mathcal{L}\left(\mathbf{F}^r\right) = \sum_{n=1}^{N_{\mathrm{atom}}^r} \sum_{\alpha=1}^{3} \left(F_{\alpha,n}^r - F_{\alpha,n}^{\mathrm{ref},r}\right)^2 \ . \qquad (3)$$

We apply here the squared deviation between predicted and reference values. The loss of energy and forces can be balanced by the hyperparameter q. Consequently, the representation quality can also be assessed by a loss vector $\mathbf{L}$ containing the contributions of each structure separately. To address the representation quality, we further split the loss contributions of energy and forces in the vectors $\mathbf{L}^E$ and $\mathbf{L}^F$, whereby, compared to the total loss L_{total}, the energy contributions are not divided by N_{fit} and the force contributions are divided by N_{atom}^r instead of $N_{\mathrm{atom}}^{\mathrm{fit,sum}}$. The latter is the total number of all atoms in all structures to be fitted.

The main difference of the lADS algorithm presented in this work compared to its original implementation in Reference [47] is (I) the separate consideration of energy and force loss contributions. (II) the advanced algorithm adjusts the number of fitted structures per training step. (III) it employs an improved scheme to calculate the training probabilities and (IV) to update the selection determining properties. (V) it includes a maximum number of structures that can be classified as redundant per step and (VI) adds a scheme for fast integration of additional training data. In addition, (VII) it enables removing loss gradient contributions of inconsistent training data in the history of the CoRe optimizer.

Algorithm 1: Selection of a training data subsample which will be fitted in the training epoch. We note that in all algorithm notations the vector operations are element-wise and assignments including conditions affect only vector entries which fulfill the conditions.

$N_{\mathrm{fit}} \leftarrow \max\left[1,\ \lfloor p_{\mathrm{fit}} \cdot \dim\left(\mathbf{S}_{\mathrm{hist}}^{>0,E}\right)\rfloor\right]$
$N_{\mathrm{good}} \leftarrow \lfloor p_{\mathrm{good}} \cdot N_{\mathrm{fit}} \rfloor$
$N_{\mathrm{bad}} \leftarrow N_{\mathrm{fit}} - N_{\mathrm{good}}$
$L_{\mathrm{old}}^{\max,E/F} \leftarrow \max\left(\mathbf{L}_{\mathrm{old}}^{\setminus \mathrm{NaN}, S_{\mathrm{hist}}^{r,E}>0,E/F}\right)$
if $L_{\mathrm{old}}^{\max,E/F} > 0$
    $\mathbf{P}_{\mathrm{loss}}^{E/F} \leftarrow \dfrac{\mathbf{L}_{\mathrm{old}}^{E/F}}{L_{\mathrm{old}}^{\max,E/F}}$
    $\mathbf{P}_{\mathrm{loss}}^{E/F} \leftarrow \dfrac{\overline{L}_{\mathrm{old}}^{E/F}}{L_{\mathrm{old}}^{\max,E/F}}$ if $P_{\mathrm{loss}}^{r,E/F} < \dfrac{\overline{L}_{\mathrm{old}}^{E/F}}{L_{\mathrm{old}}^{\max,E/F}}$
else
    $\mathbf{P}_{\mathrm{loss}}^{E/F} \leftarrow \mathbf{1}$
$\mathbf{P}_{\mathrm{loss}} \leftarrow \left(\mathbf{P}_{\mathrm{loss}}^{E} \cdot \mathbf{P}_{\mathrm{loss}}^{F}\right)^{\frac{1}{2}}$
$\mathbf{P}_{\mathrm{bad}} \leftarrow \mathbf{S}_{\mathrm{hist}}^{E} \cdot \left|\mathbf{S}_{\mathrm{hist}}^{F}\right| \cdot \mathbf{P}_{\mathrm{loss}}$
$P_{\mathrm{bad}}^{\max} \leftarrow \max\left[S_{\mathrm{hist}}^{\max},\ \max\left(\mathbf{P}_{\mathrm{bad}}^{\setminus \mathrm{NaN}}\right)\right]$
$\mathbf{P}_{\mathrm{bad}} \leftarrow P_{\mathrm{bad}}^{\max}$ if $P_{\mathrm{bad}}^{r} = \mathrm{NaN}$
$\mathbf{P}_{\mathrm{bad}} \leftarrow 0$ if $S_{\mathrm{hist}}^{r,E} \leq 0$
$\mathbf{P}_{\mathrm{bad}} \leftarrow \dfrac{\mathbf{P}_{\mathrm{bad}}}{\mathrm{sum}\left(\mathbf{P}_{\mathrm{bad}}\right)}$
$\mathbf{D}_{\mathrm{fit}} \leftarrow \mathrm{random_choice}\left(\mathbf{D},\ \mathbf{P}_{\mathrm{bad}},\ N_{\mathrm{bad}}\right)$
$\mathbf{P}_{\mathrm{good}} \leftarrow \mathbf{S}_{\mathrm{hist}}^{\setminus \mathrm{fit},E} \cdot \left|\mathbf{S}_{\mathrm{hist}}^{\setminus \mathrm{fit},F}\right| \cdot \left(1 - \mathbf{P}_{\mathrm{loss}}^{\setminus \mathrm{fit}}\right)$
$P_{\mathrm{good}}^{\min} \leftarrow \min\left[S_{\mathrm{hist}}^{\min},\ \min\left(\mathbf{P}_{\mathrm{good}}^{\setminus \mathrm{NaN},>0}\right)\right]$
$\mathbf{P}_{\mathrm{good}} \leftarrow P_{\mathrm{good}}^{\min}$ if $P_{\mathrm{good}}^{r} = \mathrm{NaN} \vee P_{\mathrm{loss}}^{\setminus \mathrm{fit},r} = 1$
$\mathbf{P}_{\mathrm{good}} \leftarrow 0$ if $S_{\mathrm{hist}}^{\setminus \mathrm{fit},r,E} \leq 0$
$\mathbf{P}_{\mathrm{good}} \leftarrow \dfrac{\mathbf{P}_{\mathrm{good}}}{\mathrm{sum}\left(\mathbf{P}_{\mathrm{good}}\right)}$
$\mathbf{D}_{\mathrm{fit}} \leftarrow \mathbf{D}_{\mathrm{fit}} \cup \mathrm{random_choice}\left(\mathbf{D}^{\setminus \mathrm{fit}},\ \mathbf{P}_{\mathrm{good}},\ N_{\mathrm{good}}\right)$

Choice of Data to be Fitted

The selection of the training structures to be fitted is given in Algorithm 1 and will be explained step-by-step in this paragraph. In each training step, the lADS algorithm utilizes a fraction of p_{fit} of all training structures that are still available for training, i.e., structures r with an adaptive selection factor $S_{\mathrm{hist}}^{r,E}$ larger than zero. In general, these adaptive selection factors determine the training probability. They incorporate the representation quality history for the energy and forces of each structure. The starting value for each structure is $S_{\mathrm{hist}}^{r,E/F} = 1$. From the N_{fit} structures, a fraction of p_{good} is selected from well represented structures, while the remaining N_{bad} structures are not yet well represented. p_{good} is initialized before the first step as zero and will be adapted as shown in Algorithm 2. By employing good and bad data, the

stability–plasticity balance of retaining old expertise and integrating new knowledge can be improved. Moreover, this approach is required for lADS to sort out redundant, well represented data.

To obtain the training probabilities, the maximum loss contributions for energies and forces $L_{\text{old}}^{\max,E/F}$ are determined among all previously calculated loss contributions of structures available for training. We note that the loss vectors $\mathbf{L}_{\text{old}}^{E/F}$ are initialized before the first step as **NaN**, i.e., a vector of not a number (NaN) entries. If there is at least one structure with a loss contribution greater than zero, the probability based on the loss $\mathbf{P}_{\text{loss}}^{E/F}$ is calculated as the loss vector divided by the maximum loss contribution. Thereby, the minimum value is set to the mean loss contribution $\overline{L}_{\text{old}}^{E/F}$ divided by the maximum loss contribution. The mean loss contributions for energy and forces are initialized before the first step as infinity. $\mathbf{P}_{\text{loss}}^{E/F}$ increases the probability that badly represented structures are selected, while providing equal probabilities for well represented structures so that even very well represented structures have a chance of being selected. If no loss contribution is greater than zero, $\mathbf{P}_{\text{loss}}^{E/F} = \mathbf{1}$ is applied. The probability vectors for energy and forces are multiplied and their square root is taken, resulting in $\mathbf{P}_{\text{loss}}$. Subsequently, $\mathbf{P}_{\text{loss}}$ is multiplied by the adaptive selection factor vectors of energies and forces. While $\mathbf{P}_{\text{loss}}$ contains information about the current representation quality, the adaptive selections factors account for the history of the representation quality. The maximum value of the resulting vector $\mathbf{P}_{\text{bad}}$ is determined to be $P_{\text{bad}}^{\max}$ that has a lower bound of $S_{\text{hist}}^{\max}$. The latter also defines the maximum value in $\mathbf{S}_{\text{hist}}$. All NaN in $\mathbf{P}_{\text{bad}}$ are set to $P_{\text{bad}}^{\max}$, i.e., structures trained for the first time have the highest probability in P_{bad}. For unavailable training structures, the respective vector entries are set to zero. The final probability is obtained by dividing the vector by the sum of its entries. Afterwards, N_{bad} structures are randomly selected from the training data D, with the respective probabilities $\mathbf{P}_{\text{bad}}$.

To choose the N_{good} structures, $1 - \mathbf{P}_{\text{loss}}$ is multiplied by the adaptive selection factor vectors for those structures that were not yet selected, resulting in $\mathbf{P}_{\text{good}}$. Therefore, high loss contributions lead to a lower probability in this case. The minimum value larger than 0 is determined as $P_{\text{good}}^{\min}$ that has an upper bound of $S_{\text{hist}}^{\min}$. The latter also defines the minimum value of the adaptive selection factor of the structures available for training. $P_{\text{good}}^{\min}$ will be employed in $\mathbf{P}_{\text{good}}$ if the vector entry is NaN or the respective P_{loss}^{r} is 1, i.e., structures trained for the first time and those with the highest loss have the lowest probability in P_{good}. Analogously to $\mathbf{P}_{\text{bad}}$, $\mathbf{P}_{\text{good}}$ is set to zero for unavailable structures, and it is divided by the sum of its entries. Finally, the resulting random training data choice using the probabilities $\mathbf{P}_{\text{good}}$ is combined with the data selected using $\mathbf{P}_{\text{bad}}$.

Update of Selection Properties

Algorithm 2: Update of the selection-determining properties.

$\mathbf{L}_{\text{new}}^{E} \leftarrow q \cdot \mathcal{L}\left(\dfrac{\mathbf{E}^{\text{fit}}}{\mathbf{N}_{\text{atom}}^{\text{fit}}}\right)$

$\mathbf{L}_{\text{new}}^{F} \leftarrow \dfrac{\mathcal{L}\left(\mathbf{F}^{\text{fit}}\right)}{3\mathbf{N}_{\text{atom}}^{\text{fit}}}$

for i in $\{1, 2, 3, 4\}$

$\quad \mathbf{L}_{Ti}^{E} \leftarrow q \cdot \mathcal{L}\left(\dfrac{T_i \cdot \mathbf{E}^{\text{fit}}}{\mathbf{N}_{\text{atom}}^{\text{fit}}}\right)$

$\quad \mathbf{L}_{Ti}^{F} \leftarrow \dfrac{\mathcal{L}\left(T_i \cdot \mathbf{F}^{\text{fit}}\right)}{3\mathbf{N}_{\text{atom}}^{\text{fit}}}$

$\quad \overline{L}_{Ti}^{E/F} \leftarrow \text{mean}\left(\mathbf{L}_{Ti}^{\backslash \text{NaN}, S_{\text{hist}}^{r,E} \geq -1, E/F}\right)$

$\mathbf{X} \leftarrow X^r + 1 \;\text{ if }\; L_{\text{new}}^{r,E} > \overline{L}_{T4}^{E} \vee L_{\text{new}}^{r,F} > \overline{L}_{T4}^{F}$

$\mathbf{X} \leftarrow 0 \;\text{ if }\; L_{\text{new}}^{r,E} \leq \overline{L}_{T4}^{E} \wedge L_{\text{new}}^{r,F} \leq \overline{L}_{T4}^{F}$

$\mathbf{S}_{\text{hist}}^{E/F} \leftarrow \max\left(1,\ S_{\text{hist}}^{r,E/F}\right) \;\text{ if }\; L_{\text{new}}^{r,E/F} \geq \overline{L}_{T1}^{E/F}$

$\mathbf{S}_{\text{hist}}^{E/F} \leftarrow \min\left(S_{\text{hist}}^{r,E/F},\ 1\right) \;\text{ if }\; L_{\text{new}}^{r,E/F} \leq \overline{L}_{T2}^{E/F}$

$\mathbf{S}_{\text{hist}}^{E/F} \leftarrow S_{\text{hist}}^{r,E/F} \cdot F_{--} \;\text{ if }\; L_{\text{new}}^{r,E/F} < \overline{L}_{T1}^{E/F} \wedge L_{\text{new}}^{r,E/F} \leq L_{\text{old}}^{r,E/F}$

$\mathbf{S}_{\text{hist}}^{E/F} \leftarrow S_{\text{hist}}^{r,E/F} \cdot F_{-} \;\text{ if }\; L_{\text{new}}^{r,E/F} < \overline{L}_{T1}^{E/F} \wedge L_{\text{new}}^{r,E/F} > L_{\text{old}}^{r,E/F}$

$\mathbf{S}_{\text{hist}}^{E/F} \leftarrow S_{\text{hist}}^{r,E/F} \cdot F_{+} \;\text{ if }\; \overline{L}_{T2}^{E/F} < L_{\text{new}}^{r,E/F} \leq \overline{L}_{T3}^{E/F} \wedge L_{\text{new}}^{r,E/F} > L_{\text{old}}^{r,E/F}$

$\mathbf{S}_{\text{hist}}^{E/F} \leftarrow S_{\text{hist}}^{r,E/F} \cdot F_{+} \;\text{ if }\; L_{\text{new}}^{r,E/F} > \overline{L}_{T3}^{E/F} \wedge L_{\text{new}}^{r,E/F} \leq L_{\text{old}}^{r,E/F}$

$\mathbf{S}_{\text{hist}}^{E/F} \leftarrow S_{\text{hist}}^{r,E/F} \cdot F_{++} \;\text{ if }\; L_{\text{new}}^{r,E/F} > \overline{L}_{T3}^{E/F} \wedge L_{\text{new}}^{r,E/F} > L_{\text{old}}^{r,E/F}$

$\mathbf{S}_{\text{hist}}^{E/F} \leftarrow -3 \;\text{ if }\; X^r \geq N\mathbf{X}$

$\mathbf{S}_{\text{hist}}^{E/F} \leftarrow -2 \;\text{ if }\; \left[\max\left(0,\ S_{\text{hist}}^{r,E} - 1\right)\right]^2 + \left[\max\left(0,\ S_{\text{hist}}^{r,F} - 1\right)\right]^2 > \left(S_{\text{hist}}^{\max} - 1\right)^2$

$\mathbf{S}_{\text{hist}}^{E/F} \leftarrow -1 \;\text{ if }\; \left\{\max\left[0,\ \left(S_{\text{hist}}^{r,E}\right)^{-1} - 1\right]\right\}^2 + \left\{\max\left[0,\ \left(S_{\text{hist}}^{r,F}\right)^{-1} - 1\right]\right\}^2 > \left[\left(S_{\text{hist}}^{\max}\right)^{-1} - 1\right]^2$

$\mathbf{L}_{\text{old}}^{\text{fit,E/F}} \leftarrow \mathbf{L}_{\text{new}}^{E/F}$

$\overline{L}_{\text{new}}^{E/F} \leftarrow \text{mean}\left(\mathbf{L}_{\text{old}}^{\backslash \text{NaN}, S_{\text{hist}}^{r,E} \geq -1, E/F}\right)$

if $\overline{L}_{\text{new}}^{E} \leq \overline{L}_{\text{old}}^{E} \wedge \overline{L}_{\text{new}}^{F} \leq \overline{L}_{\text{old}}^{F}$

$\quad p_{\text{good}} \leftarrow \max\left(0,\ p_{\text{good}} - \dfrac{p_{\text{good}}^{\max}}{N_p}\right)$

else

$\quad p_{\text{good}} \leftarrow \min\left(p_{\text{good}} + \dfrac{p_{\text{good}}^{\max}}{N_p},\ p_{\text{good}}^{\max}\right)$

$\overline{L}_{\text{old}}^{E/F} \leftarrow \overline{L}_{\text{new}}^{E/F}$

To update the selection-determining properties (Algorithm 2), the loss contributions $\mathbf{L}_{\text{new}}^{E/F}$ of the currently chosen structures are calculated. In addition, loss contributions $\mathbf{L}_{Ti}^{E/F}$ are calculated for which the deviation is scaled by one of four threshold factors T_i, with $i = 1, 2, 3, 4$. These vectors are initialized before the first step

as **NaN**. For each of these vectors the mean $\overline{L}_{Ti}^{E/F}$ is determined for available structures and those assigned to be redundant.

If the new energy or force loss contribution of a structure r is larger than the mean loss contribution applying the largest threshold factor $\overline{L}_{T4}^{E/F}$, then the exclusion strike counter X^r of that structure will be increased by one. The starting value of this counter is zero for each structure. If the loss contributions for energy and forces are lower than the threshold, then the counter will be reset to zero. Afterwards, the adaptive selection factors $S_{\text{hist}}^{r,E/F}$ are individually updated for energies and forces. If the new loss contribution $L_{\text{new}}^{r,E/F}$ is not lower than the first threshold $\overline{L}_{T1}^{E/F}$, $S_{\text{hist}}^{r,E/F}$ will have a lower bound of one. An upper bound of one will be applied if the value is not higher than the second threshold $\overline{L}_{T2}^{E/F}$. In this way, only well/bad represented structures can get a small/large $S_{\text{hist}}^{r,E/F}$ value, while the $S_{\text{hist}}^{r,E/F}$ values of structures with intermediate representation quality retain around one. Subsequently, $S_{\text{hist}}^{r,E/F}$ is modified by large and small decrease factors F_{--} and F_{-} as well as small and large increase factors F_{+} and F_{++} depending on the value of the new loss contribution $L_{\text{new}}^{r,E/F}$ compared to the threshold values $\overline{L}_{Ti}^{E/F}$ and the old loss contribution $L_{\text{old}}^{r,E/F}$. These decrease and increase factors are calculated from the hyperparameters $N_{-/--}$ and $N_{+/++}$ by $F_{-/--} = (S_{\min})^{(N_{-/--})^{-1}}$ and $F_{+/++} = (S_{\max})^{(N_{+/++})^{-1}}$. Therefore, $N_{-/--}$ and $N_{+/++}$ define the number of repeated applications of the respective factor until $S_{\min}$ or $S_{\max}$ is reached. Exceeding these lower and upper bounds leads to the exclusion of the associated structure from training, as described below.

If the exclusion strike counter X^r reaches its limit $N_{\mathbf{X}}$, $S_{\text{hist}}^{r,E/F}$ is set to -3 and the structure is excluded due to very large errors. If the upper threshold for S_{hist}^{r} as defined in Algorithm 2 is exceeded, -2 is assigned to $S_{\text{hist}}^{r,E/F}$ to exclude the structure due to steadily large errors for many training steps. Both assignments mean that the respective training data point is inconsistent with the majority of data. If the lower threshold for S_{hist}^{r} is exceeded, $S_{\text{hist}}^{r,E/F}$ is set to -1, classifying a redundant structure, i.e., a structure that has been well represented for many steps. To avoid that too many structures are classified as redundant in the same training step, a maximal fraction of the new redundant training structure per step $p_{\text{redun}}^{\max}$ can be set in addition to Algorithm 2. In this way, only

$$N_{\text{redun}}^{\max} = \max\left(1,\ \lceil p_{\text{redun}}^{\max} \cdot N_{\text{fit}} \rceil\right) \tag{4}$$

randomly selected structures of all structures exceeding the lower threshold are assigned to be redundant and $S_{\text{hist}}^{r,E/F}$ of the remaining structures is divided by F_{--}.

To update the fraction of good data p_{good}, the new loss contributions first replace the respective old ones in $\mathbf{L}_{\text{old}}^{E/F}$. Subsequently, the mean $\overline{L}_{\text{new}}^{E/F}$ of this vector is calculated for all available training data and those assigned to be redundant. If the new means of energies and forces are not larger than the respective old values, p_{good} will decrease by $p_{\text{good}}^{\max} N_p^{-1}$. Otherwise, it increases by the same value. The resulting p_{good} has a lower bound of 0 and an upper bound of $p_{\text{good}}^{\max}$. Consequently, p_{good} can have N_p+1 different values. Finally, $\overline{L}_{\text{old}}^{E/F}$ is overwritten by $\overline{L}_{\text{new}}^{E/F}$.

Integration of New Data

For an efficient integration of additional data at a training stage where some structures are already well represented, Algorithm 3 can replace lines 3 to 6 of Algorithm 2. The main idea behind this data integration is that the additional data can have the maximum training probability for several training steps, while they cannot be excluded during these steps. In this way, the lMLP can learn the new structures fast, even if the representation quality is very different between the previous and new training data. Without this integration algorithm, the risk of exclusion is high for new data because the typically low errors for the majority of old data lead to a fast increase in the exclusion strike counters and the adaptive selection factors of new data with high errors. In addition, the new data initially do not affect the update of the selection-determining properties of the old data to obtain a stable assessment of the representation quality.

Algorithm 3: Integration of new training data.

for i in $\{1,2,3,4\}$

$\quad \mathbf{L}_{Ti}^{E} \leftarrow q \cdot \mathcal{L}\left(\dfrac{T_i \cdot \mathbf{E}^{\text{fit}}}{\mathbf{N}_{\text{atom}}^{\text{fit}}}\right)$ if $L_{\text{old}}^{r,E} \neq \text{NaN}$

$\quad \mathbf{L}_{Ti}^{F} \leftarrow \dfrac{\mathcal{L}\left(T_i \cdot \mathbf{F}^{\text{fit}}\right)}{3\mathbf{N}_{\text{atom}}^{\text{fit}}}$ if $L_{\text{old}}^{r,E} \neq \text{NaN}$

$\quad \overline{L}_{Ti}^{E/F} \leftarrow \text{mean}\left(\mathbf{L}_{Ti}^{\setminus \text{NaN}, S_{\text{hist}}^{r,E} \geq -1, E/F}\right)$

$\mathbf{I} \leftarrow I^r + 1$ if $\left(L_{\text{new}}^{r,E} > \overline{L}_{T2}^{E} \vee L_{\text{new}}^{r,F} > \overline{L}_{T2}^{F}\right) \wedge L_{\text{old}}^{r,E} = \text{NaN}$

$\mathbf{I} \leftarrow 0$ if $L_{\text{new}}^{r,E} \leq \overline{L}_{T2}^{E} \wedge L_{\text{new}}^{r,F} \leq \overline{L}_{T2}^{F}$

$\mathbf{L}_{\text{new}}^{E/F} \leftarrow \text{NaN}$ if $0 < I^r < N_{\mathbf{I}}$

In contrast to Algorithm 2, Algorithm 3 does not consider loss contributions of structures evaluated for the first time ($L_{\text{old}}^{r,E} = \text{NaN}$) in the calculation of the loss contribution threshold values. In this way, we circumvent the effect that most old structures will be considered as relatively well represented just because new structures with typically high errors have been added. Algorithm 3 introduces the integration counter I^r, which is initialized as zero for each structure. It is increased by one in every training step of a new structure, which still has an energy or force loss contribution greater than the second lowest threshold. If the latter condition is not satisfied,

I^r is set to zero. Subsequently, the loss contribution of new structures with high errors ($I^r > 0$) will be reset to NaN if the integration counter is still below the maximum number of integration steps $N_\mathbf{I}$. This reset retains the classification of a structure to be new and the associated maximum training probability. In this way, new structures are integrated into the general selection process as soon as their accuracy is close to those of the majority of the data, while inconsistent data cannot get stuck in this integration process.

Backtracking Loss Gradients of Inconsistent Data

Many optimizers utilize the momentum of the optimization process to achieve better performance [55]. For example, Adam [66] and the CoRe optimizer [47, 55] employ the exponential moving average of the loss gradient in the model parameter update to consider the loss gradient history. As a consequence, the loss gradient contributions of inconsistent training data can affect the optimization process even after these data have been excluded from training. To counteract this effect, we propose Algorithm 4 for backtracking loss gradient contributions of inconsistent training data in the CoRe optimizer. This algorithm basically eliminates contributions of training data which have been classified to be inconsistent. We note that Algorithm 4 is optimizer-specific because the optimizer algorithm determines the weight of individual loss gradient contributions in the employed gradient for model parameter updates.

To determine the weight of the loss gradient contribution for a given structure in the exponential moving average, we need to know in which training steps this structure has been utilized and how large the respective loss function gradient contribution was. To avoid saving this large amount of data for all training data, Algorithm 4 estimates the most probable steps based on a few assumptions and employs the current loss function gradient. First, we assume that a structure is excluded due to errors larger than threshold 3 for N_{++} steps or larger than threshold 4 for $N_\mathbf{X}$ steps. The $S_\text{hist}^{r,E/F}$ value of inconsistent data reveals which of the two cases applies. Moreover, we assume that either only energy errors or only force errors exceed the threshold. To estimate the training probability, all values of the respective adaptive selection factors $\mathbf{F_S}$ and $\mathbf{F_X}$ are calculated for both cases. In addition, the non-normalized probabilities $\mathbf{P}^\text{sum}$ need to be determined for all other training data that are still available for training. Therefore, we assume that their current adaptive selection factors and probabilities based on the loss are also a reasonable representation for previous steps, and we estimate the ratio of well and badly represented data by the current p_good value. P_bad^max is utilized if $P^{\text{sum},r}$ equals NaN. In the remaining algorithm, only the sum P^sum is required.

The following part of Algorithm 4 has to be repeated for each structure r' that has been identified in the current step to be inconsistent. Initially, the non-normalized probabilities $\mathbf{P}^{r'}$ are calculated using the current $P_\text{loss}^{r'}$ and p_good and $\mathbf{F_S}$ or $\mathbf{F_X}$. The latter depends on which exclusion reason applies for r'. Afterwards, the average training frequency is calculated for each entry in $\mathbf{P}^{r'}$, whereby a structure can only be trained once in a training step. The cumulative sum minus the value of the first vector entry yields the vector of backtracking steps $\mathbf{t}_\text{BT}$. The current epoch n_epoch minus $\mathbf{t}_\text{BT}$ corresponds to the most probable training steps of structure r' under the aforementioned assumptions. For these steps, the decay hyperparameters $\boldsymbol{\beta}_1$ of the CoRe optimizer are calculated. Subsequently, the backtracking factors F_BT^1 and F_BT^2 can be obtained, i.e., the sum of the weights of all loss gradient contributions of structure r' in the steps $n_\text{epoch} - \mathbf{t}_\text{BT}$ can be calculated using the decay hyperparameters $\boldsymbol{\beta}_1$ and β_2.

Finally, we assume that the loss contribution $L^{r'}$ after the model parameter update is also a reasonable representation of the previous loss contributions. We note that recent loss gradients contribute the most, which supports

Algorithm 4: Backtracking loss gradients of inconsistent training data r' in the history of the CoRe optimizer.

$$\mathbf{F_S} \leftarrow S_\text{hist}^\text{max} \left[(S_\text{hist}^\text{max})^{\frac{(0,1,\ldots,N_{++}-1)^\text{T}}{N_{++}}} \right]^{-1}$$

$$S_\text{hist}^{\text{max},\mathbf{X}} \leftarrow (S_\text{hist}^\text{max})^{\frac{N_\mathbf{X}}{N_{++}}}$$

$$\mathbf{F_X} \leftarrow S_\text{hist}^{\text{max},\mathbf{X}} \left[\left(S_\text{hist}^{\text{max},\mathbf{X}}\right)^{\frac{(0,1,\ldots,N_\mathbf{X}-1)^\text{T}}{N_{++}}} \right]^{-1}$$

$$\mathbf{P}^\text{sum} \leftarrow \mathbf{S}_\text{hist}^{>0,E} \cdot \mathbf{S}_\text{hist}^{>0,F} \cdot \Big[(1-p_\text{good})\, \mathbf{P}_\text{loss}^{S_\text{hist}^{r,E}>0} + p_\text{good} \left(1 - \mathbf{P}_\text{loss}^{S_\text{hist}^{r,E}>0}\right) \Big]$$

$$\mathbf{P}^\text{sum} \leftarrow P_\text{bad}^\text{max} \;\text{ if }\; P^{\text{sum},r} = \text{NaN}$$

$$P^\text{sum} \leftarrow \text{sum}\left(\mathbf{P}^\text{sum}\right)$$

$$\mathbf{P}^{r'} \leftarrow \mathbf{F}_{\mathbf{S}\vee\mathbf{X}} \left[(1-p_\text{good})\, P_\text{loss}^{r'} + p_\text{good} \left(1 - P_\text{loss}^{r'}\right) \right]$$

$$\mathbf{t}_\text{BT} \leftarrow \text{cumsum}\left\{ \left[\min\left(\frac{N_\text{fit} \cdot \mathbf{P}^{r'}}{P^\text{sum} + \mathbf{P}^{r'}},\; 1 \right) \right]^{-1} \right\}$$

$$\mathbf{t}_\text{BT} \leftarrow \mathbf{t}_\text{BT} - t_0$$

$$\boldsymbol{\beta}_1 \leftarrow \beta_1^\text{b} + \left(\beta_1^\text{a} - \beta_1^\text{b}\right) \exp\left[-\left(\frac{n_\text{epoch} - \mathbf{t}_\text{BT}}{\beta_1^\text{c}} \right)^2 \right]$$

$$F_\text{BT}^1 \leftarrow \text{sum}\left[(1-\boldsymbol{\beta}_1) \cdot (\boldsymbol{\beta}_1)^{\mathbf{t}_\text{BT}} \right]$$

$$F_\text{BT}^2 \leftarrow \text{sum}\left[(1-\beta_2) \cdot (\beta_2)^{\mathbf{t}_\text{BT}} \right]$$

$$L^{r'} \leftarrow \frac{q}{N_\text{fit}} \cdot \mathcal{L}\left(\frac{E^{r'}}{N_\text{atom}^r} \right) + \frac{\mathcal{L}\left(\mathbf{F}^{r'}\right)}{3N_\text{atom}^\text{fit,sum}}$$

$$\mathbf{g} \leftarrow \mathbf{g} - F_\text{BT}^1 \cdot \frac{\partial L^{r'}}{\partial \mathbf{w}}$$

$$\mathbf{h} \leftarrow \mathbf{h} - F_\text{BT}^2 \cdot \left(\frac{\partial L^{r'}}{\partial \mathbf{w}} \right)^2$$

$$\mathbf{h} \leftarrow 0 \;\text{ if }\; h^\xi < 0$$

this approximation. We calculate the gradient of $L^{r'}$ with respect to the model parameters $\mathbf{w}$ and its square and subtract these gradients weighted by the respective backtracking factors from the exponential moving averaged loss gradient $\mathbf{g}$ and squared loss gradient $\mathbf{h}$ in the CoRe optimizer. In this way, the loss gradient contributions of structure r' are eliminated. Since this algorithm is approximate, we enforce the required condition that values h^{ξ} in $\mathbf{h}$ cannot be lower than 0.

Since an optimization step based on energies alone can be much faster than one based on energies and forces (due to the additional differentiation step), a pre-optimization step on energies before the actual optimization step on both energy and forces can increase the training efficiency. To apply Algorithm 4 in this case, $\mathbf{t}_{\mathrm{BT}}$ needs to be multiplied by two. In addition, the Algorithm has to be repeated for the energy pre-optimization step with the modification that $\mathbf{t}_{\mathrm{BT}}$ again needs to be multiplied by a factor of two. It also needs to be increased by one, and only the energy loss contribution has to be utilized.

Hyperparameters

For the lADS hyperparameters, we recommend these settings: $p_{\mathrm{fit}} = \frac{1}{30}$, $S_{\mathrm{hist}}^{\mathrm{min}} = 0.1$, $S_{\mathrm{hist}}^{\mathrm{max}} = 100$, $T_i = \{0.9, 2.5, 4.0, 7.5\}$, $N_{--} = 10$, $N_{-} = 30$, $N_{+} = 100$, $N_{++} = 300$, $N_{\mathbf{X}} = 15$, $p_{\mathrm{redun}}^{\mathrm{max}} = 0.02$, $p_{\mathrm{good}}^{\mathrm{max}} = \frac{2}{3}$, $N_p = 20$, and $N_{\mathbf{I}} = 30$. The data integration algorithm (Algorithm 3) can be applied as soon as new data are added for the first time. Hence, Algorithm 3 needs to be disabled only if training is started from scratch. In addition, the hyperparameter for balancing the energy and force loss contributions was $q = 250$ in this work. These settings were applied unless otherwise stated.

2.3. Universal Machine Learning Potentials

The goal of uMLPs is to achieve out-of-the-box applicability for chemically meaningful structures. Then, further retraining is not necessary and expensive reference calculations can be avoided during application. To achieve this goal, models with universal structure representations are trained on very large and diverse reference data sets.

ANI [67] is one of the initial attempts to create a more general MLP. Still, the applicability of ANI-1x [63] and ANI-2x [68] are, among other restrictions, limited to four and seven chemical elements, respectively. Graph representations can remove this limitation, as demonstrated, for example, by M3GNet [44] and MACE [69]. These MLPs were trained on data from the Materials Project [70, 71] and can be universally applied to almost the entire periodic table. In recent years, many more general and universal models have been proposed, such as ANI-1xnr [72], AIMNet2 [73], TeaNet [74], PreFerred Potential [75], TeaNet/PreFerred Potential [76], ALIGNN-FF [77], GNoME [78], MatterSim [79], and CHGNet [80] (in increasing order of covered elements).

Current uMLPs have already shown remarkable success in various benchmarks providing accurate and stable simulation results [46, 81]. However, these benchmarks have also revealed that there are still a lot of applications, for which the accuracy of the uMLPs is not sufficient and further training is required. Fine-tuning of the universal foundation models on specialized data can often be a solution to increase the accuracy to the desired level. However, to reach the final goal of out-of-the-box applicability, the diversity and size of the uMLP reference data sets needs to be increased. We note that the combination of an MLP with a semi-empirical method as in AIQM1 [82] can also increase transferability and accuracy, while computational efficiency is at an affordable level.

Beyond the applicability for different chemical elements, the total charge and spin states have to be handled by the uMLP as well. Current uMLPs are trained on data of neutral systems in the electronic ground state which compromises predictions on charged systems. In addition, for a comprehensive representation of chemical space, training data need to cover different aggregation states and various conformations of the system, including out-of-equilibrium structures. The focus of uMLPs is typically either on gas-phase molecules or on solid materials. Attempts have been made to integrate transitions between equilibrium structures in general training data sets [83].

In this work, we evaluate the general MLPs ANI-1x [63] and ANI-2x [68] and the uMLPs M3GNet-MP-2021.2.8-PES (M3GNet) [44], M3GNet-MP-2021.2.8-DIRECT-PES ($\mathrm{M3GNet_{DIRECT}}$) [84], MACE-MP-0 small, medium, and large ($\mathrm{MACE_{MP}^{s/m/l}}$) [45], and MACE-OFF23 small, medium, and large ($\mathrm{MACE_{OFF}^{s/m/l}}$) [85].

3. COMPUTATIONAL DETAILS

3.1. Exploration of Chemical Reaction Networks

For the CRN exploration we applied our freely available open-source Software for Chemical Interaction Networks (SCINE) [86], especially the SCINE modules Chemoton (version 3.0.0) [23, 87], Molassembler (version 2.0.0) [88, 89], ReaDuct (version 5.0.0) [90, 91], Puffin (version 1.2.0) [92], and Database (version 1.2.0) [93]. The required DFT calculations were carried out with the quantum chemistry software ORCA (version 5.0.3) [94, 95]. We executed spin unrestricted DFT calculations with the PBE exchange-correlation functional [96] in combination with the def2-TZVP basis set [97] and with the ωB97X functional [98] in combination with the smaller split-valence 6-31G* basis set [99]. The xTB software [100] was applied for semi-empirical GFN2-xTB calculations [101]. For MLP energy, gradient, and Hessian

calculations within SCINE, we implemented the module SCINE Parrot (version 1.0.0).

Elementary step trials in the CRN exploration employed the Newton Trajectory Algorithm 2 (NT2) of Chemoton (see Reference [23] for details). In the NT2 scans, uni- and bimolecular reactions were considered for one *structure* per *compound*, whereby multiple attack points were enabled, but at most two rotamers and two bond modifications were allowed [87]. We note that *structure* and *compound* refer here to their technical terms in SCINE [7]; that is, a *structure* is a (stationary) point on the potential energy surface and a *compound* is a group of *structures* with the same connectivity as defined in SCINE Molassembler. Reactive complexes were not generated for two charged *structures* with the same sign of the charge. The spin multiplicity of the resulting *structures* was chosen to be as small as possible. The exploration was only continued for *structures* which can be reached by an energy barrier up to $250\,\mathrm{kJ\,mol^{-1}}$. 10% of the occurring structure conformations in the NT2 scans as well as in the following intrinsic reaction coordinate (IRC) calculations were stored for the evaluation by the MLPs. In addition, 1% of the structure conformations occurring in the optimizations of reactants, reactive complexes, transition states, and IRC products were saved. The structure conformations were ordered chronologically to enable continual learning retrospectively.

3.2. Machine Learning Potentials

To evaluate general MLPs or uMLPs, we applied TorchANI (version 2.2.4) [102] for ANI-1x and ANI-2x calculations, the Materials Graph Library (MatGL) (version 0.8.5) [44] for M3GNet and $\mathrm{M3GNet_{DIRECT}}$ calculations, and MACE-Torch (version 0.3.4) [69] for $\mathrm{MACE^{\mathit{s/m/l}}_{MP/OFF}}$ calculations. We implemented training and prediction of lMLPs in the lMLP software (version 2.0.0). It utilizes NumPy (version 1.26.4) [103], PyTorch (version 2.3.1) [104], and Numba (version 0.60.0) [105].

The eeACSF parameter values of the lMLPs are provided in Tables S1 and S2 in the Supporting Information. Network expressivity by activation rank (NEAR) [106] was applied as a training-free pre-estimator of neural network performance to automate the search for the neural network architecture. The resulting architecture contains 135 input neurons, four hidden layers with 117, 137, 164, and 196 neurons, and one output neuron. The training was based on total energies, from which the sum of the respective reference element energies (Table S3 in the Supporting Information) were subtracted, and on atomic force components. For each lMLP training, we carried out 20 independent HDNNP training runs, in which the initial neural network weight parameter values and the reference data assignment to training and test sets were different. The weight parameter initialization was tailored to the activation function $\mathrm{sTanh}(x) := 1.59223 \cdot \tanh(x)$ [47]. In general, 90% of the reference structures were used for training and 10% for testing. Three different schemes for the number of fitted structures per training epoch were applied: (1) a constant fraction of $\frac{1}{30}$ of all training structures contained in the respective data set, (2) a constant number of $N_\mathrm{fit} = 750$ structures, and (3) an adjustment to the number of training structures that are not sorted out (as in Algorithm 1), with a constant fraction $p_\mathrm{fit} = \frac{1}{30}$. The hyperparameters of lADS are given in Section 2.2. Exceptions were made for scheme (1) $T_\mathrm{l} = 0.75$, $N_- = 40$, $N_{++} = 400$, and $p^\mathrm{max}_\mathrm{redun} = 0.015$, and for scheme (2) $p^\mathrm{max}_\mathrm{redun} = 0.0125$.

In the lMLP weight parameter optimization, a preoptimization step was carried out based on the energy-dependent term of the loss function L_total (Equation 1) employing each selected structure in a training epoch. Subsequently, the energy and all atomic force components of these structures were utilized in a second optimization step, which included updating the lADS properties. The CoRe optimizer (version 1.1.0) [47, 55, 107] was applied with the hyperparameters $\beta^\mathrm{a}_1 = 0.7375$, $\beta^\mathrm{b}_1 = 0.8125$, $\beta^\mathrm{c}_1 = 250.0$, $\beta_2 = 0.99$, $\epsilon = 10^{-8}$, $\eta_- = 0.55$, $\eta_+ = 1.2$, $s^0_\xi = 10^{-3}$, $s_\mathrm{min} = 10^{-6}$, $s_\mathrm{max} = 10^{-2}$, $d = 0.1$, $t_\mathrm{hist} = 250$, and $p_\mathrm{frozen} = 0.025$. Exceptions were $p_\mathrm{frozen} = 0$ and $d = 0.01$ for the weight parameters α and β (see Supporting Information S1.1) and $p_\mathrm{frozen} = 0$ and $d = 0$ for weight parameters associated with the output neuron.

The prediction was based on an ensemble of the 10 best individual HDNNPs of all 20. The respective ranking for the selection was given by the sum of the mean squared errors of the test energies and test atomic force components, whereby the energy error was scaled by $2\,500\,\mathrm{Å}^{-2}$.

4. RESULTS AND DISCUSSION

4.1. Chemical Reaction Network

We describe the CRN by technical terms of SCINE [7], where an *elementary step* is a transformation from a minimum energy *structure* to another one through a single transition state. A *reaction* is a group of *elementary steps* connecting the *structures* belonging to two reacting *compounds* (see Section 3.1). Hence, two *compounds* can be connected by a *reaction*.

Two CRN explorations were carried out starting both from HCN and H_2O. One was based on PBE/def2-TZVP energies and the other on ωB97X/6-31G* energies. Each exploration proceeded in two shells; that is, all initial elementary step trials (see Section 3.1) were calculated for HCN and H_2O, and afterwards, all subsequent trials were calculated for the *compounds* resulting from the initial trials. The resulting PBE CRN is built from 719 *compounds* and 1 230 *reactions*, while the ωB97X CRN comprises 880 *compounds* and 1 500 *reactions*. The difference in these numbers can be explained by the different potential energy surfaces represented by the different exchange-correlation density functionals, which affect the

elementary step trials and hence the applied restrictions for the exploration.

The CRN of HCN + H_2O is important in the context of the origin of life [108, 109]. The initial two steps in the formation of formic acid (up to the formation of formamide) [110] are contained in the obtained CRN. The last step is expected to be absent because only two exploration shells were considered. Other species such as hydrogen isocyanide, methylene imine, aminoacetonitrile, hydrogen peroxide, and molecular hydrogen are included in the CRN, as are many high-energy species. We note that a proper evaluation of this chemistry would require more exploration shells to fully represent the reaction mechanisms.

However, since we are interested in a typical ensemble of structures that is encountered in CRN explorations, we can limit the exploration to the first two shells. Since the structures that we encounter do not only span minimum-energy and transition-state structures, but also all sorts of positions of the atoms along (not yet optimized) reaction paths, we will call all of them 'structure conformations' or just 'conformations' for the sake of brevity in this work. Some reaction coordinates led to structures of comparatively high energies which have to be represented sufficiently well by the MLP. We compiled fractions of the structures occurring in all different exploration calculation steps in a benchmark data set (see Section 3.1). Details on the number of structures from the different calculation steps are provided in Table S4 in the Supporting Information. In total, 225 595 structures were collected from the PBE CRN and 296 093 from the ωB97X CRN.

4.2. Universal Machine Learning Potentials for Exploration of Chemical Reaction Networks

To investigate whether current uMLPs can reliably explore the HCN + H_2O CRN example, we compare their energy and force predictions for the obtained benchmark data with the DFT reference results. ANI-1x and ANI-2x were trained on ωB97X/6-31G* energies making a direct comparison with our ωB97X/6-31G* CRN results possible. M3GNet, $\text{M3GNet}_{\text{DIRECT}}$, and $\text{MACE}^{s/m/l}_{\text{MP}}$ are based on PBE energies but employ the projector augmented wave method [111] with an energy cutoff of 520 eV instead of the def2-TZVP basis set chosen for the PBE CRN exploration. Due to the different basis sets, a shift is present in the total energy. To remove this shift, we calculated element energies $\overline{E}^m_{\text{elem,diff}}$ from a least squares fit of MLP − DFT energies as a function of the respective structures' stoichiometries. The sum of these element energies,

$$E_{\text{elem}} = \sum_{m=1}^{N_{\text{elem}}} \sum_{n=1}^{N^m_{\text{atom}}} \overline{E}^m_{\text{elem,diff}} \ , \tag{5}$$

is taken as a correction in the calculation of the root mean square error (RMSE) of the given MLP energies compared to the reference DFT energies.

The resulting energy RMSEs might still show small differences from those of the actual energy reference. The reasons are that, on the one hand, the correction can compensate to some degree systematic biases of the MLP. For a fair comparison, we therefore calculated and applied this correction for every MLP. On the other hand, the shift does not account for relative changes in the potential energy surface due to the basis set change. However, all basis sets are chosen to be sufficiently accurate. Hence, only small changes in the relative energies and forces are expected. We note that $\text{MACE}^{s/m/l}_{\text{OFF}}$ is trained on ωB97M-D3(BJ)/def2-TZVPPD energies [112–115] and compared to ωB97X/6-31G* CRN data. Consequently, relative energy differences can be larger, and the interpretation of these data must be taken with care.

To enable reliable kinetic modeling based on the CRN energies, we require at least chemical accuracy, i.e., $1\,\text{kcal}\,\text{mol}^{-1} = 4.184\,\text{kJ}\,\text{mol}^{-1}$, or better. Since the benchmark data contains systems with up to 12 atoms, a minimum energy accuracy of about $3.614\,\text{meV}\,\text{atom}^{-1}$ must be the target. However, the uMLP energies show RMSEs of at least several tens of $\text{meV}\,\text{atom}^{-1}$ (Figure 3 (a)), which is an order of magnitude higher than the target. We note that this relative energy difference is also more than an order of magnitude larger than expected if a sufficiently large basis set is replaced by another sufficiently large basis set.

Similarly, the MLP accuracy target of $100\,\text{meV}\,\text{Å}^{-1}$ for the atomic force components [58] cannot be achieved by the uMLPs for these CRN benchmark data (Figure 3 (b)). Not surprisingly, HCN + H_2O CRN explorations based on ANI-2x and M3GNet energies fail because they yield too often unphysical chemical structures and energy profiles. Consequently, the uMLPs investigated are not truly universal and not yet accurate enough for the CRN exploration considered here.

4.3. Reference Data for the Lifelong Machine Learning Potential

To increase the accuracy, training on system-specific data can be a solution. To show that an MLP is in principle able to yield the desired accuracy, we trained an lMLP on the PBE data. Moreover, this large data set allows us to evaluate the performance of continual learning algorithms. These algorithms are necessary for the final goal of rolling explorations, which is the standard setting of an exploratory approach towards chemical reactivity as it may face new reactants, new catalysts, new reductants or oxidants, and so forth, that might not have been well represented by the (initial) training data set. Hence, the lMLP has been designed to efficiently and continuously improve on the fly with new training data getting

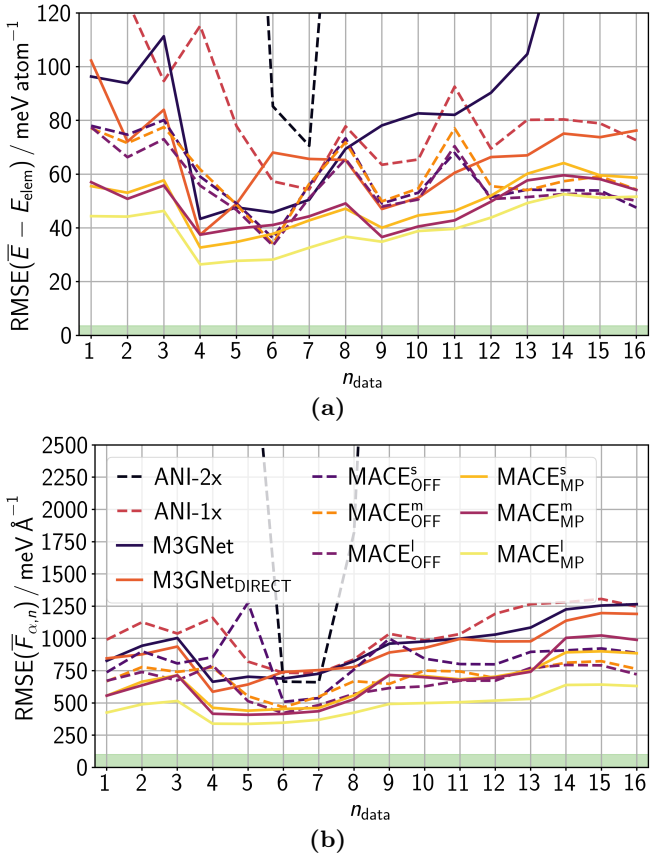

Figure 3: RMSEs of **(a)** energies $\overline{E}$ corrected by E_{elem} and **(b)** atomic force components $\overline{F}_{\alpha,n}$ evaluated using different general and universal MLPs on the CRN benchmark data. The data set was split into 16 chronologically ordered sets of equal size. In this figure and in Figures 8 and 9 below, lines are shown to guide the eye, but only values at integer numbers of n_{data} are meaningful. The RMSE interval shaded in green represents the accuracy aimed for. MACE$^{s/m/l}_{\text{OFF}}$ results are compared with ωB97X instead of ωB97M-D3(BJ) data.

absorbed (and redundant old data getting forgotten) during the exploration [47] .

The lMLP is typically trained on the difference of the total energy and the sum of reference element energies. These reference element energies differ from the element energies of the previous section in that they are determined before training on some reference structures. In this work, the reference element energies $E^{\text{ref}}_{\text{elem}}$ are calculated from a least squares fit of the total energies of H_2, CH_4, NH_3, and H2O as a function of their stoichiometries. These reference element energies are applied in Table 1 to show the range and standard deviation of the energies without atomic contributions and atomic force components for the benchmark data.

To further increase the accuracy of the lMLP, we train the lMLP on the energy difference of PBE DFT energies

Table 1: Numbers of structure conformations N_{conf}, as well as ranges and standard deviations of energies $E - E^{\text{ref}}_{\text{elem}}$ and atomic force components $F_{\alpha,n}$ are given for the different data sets.

	PBE − GFN2	PBE	ωB97X
N_{conf}	225 543	225 045	294 916
$\left(E - E^{\text{ref}}_{\text{elem}}\right)^{\text{range}}$ / meV atom^{-1}	1 578.2	4 076.5	6 159.3
$\left(E - E^{\text{ref}}_{\text{elem}}\right)^{\text{std}}$ / meV atom^{-1}	61.0	131.0	151.7
$F^{\text{range}}_{\alpha,n}$ / meV Å^{-1}	8 717	29 913	29 833
$F^{\text{std}}_{\alpha,n}$ / meV Å^{-1}	649	448	560

and GFN2 semi-empirical energies. We note that the semi-empirical method can be replaced by another fast base model. However, the method should not restrict the application range (by contrast to what hampers, for instance, non-reactive force fields), and the difference in the potential energy surface should not be too large, since otherwise the benefit vanishes. For example, a very simple Mie potential with a cutoff radius and parameters trained on DFT data did not improve the results. The advantage of this Δ-learning approach can already be seen in Table 1 because the energy and force ranges are significantly smaller than those of the pure PBE data. Smaller ranges can facilitate the achievement of higher absolute prediction accuracy, since the same relative error leads to a smaller absolute error. We note that structures with absolute atomic force components larger than 4.45 meV Å^{-1} for PBE − GFN2 and 15 meV Å^{-1} for PBE and ωB97X were excluded from the performance evaluation, as the accurate prediction of highly unstable structures is not relevant in the application for CRNs. This exclusion also applies to Figures 3 (a) and (b). Consequently, we removed the respective structures for lMLP training. Despite the smaller threshold in the case of PBE − GFN2, more structures were excluded for PBE.

4.4. Iterative Learning vs. Continual Learning

We first evaluate the performance of the continual learning algorithms to demonstrate that lMLPs can, in principle, be applied in rolling CRN explorations. Only afterwards, we consider lifelong adaptive data selection to reduce the amount of training data considered, and then, in Section 4.6, we investigate whether the lMLP also reaches the target accuracy for CRN energies.

In an lMLP-driven exploration, the lMLP is be pretrained on an initial data set and then continuously trained on additional, initially unknown data that are flowing in. We constructed a reproducible setting for an exploration process in the following way: We ordered the CRN data by their occurrence during the DFT explo-

ration process and split them into N_{data} equally sized sets. Hence, the structures in the initial set represent reactions between HCN and H_2O, while those of the final sets contain reactions between larger and more complex molecules. For simplicity, we started the performance evaluation by training an lMLP from scratch on the first set and then continuously trained one set after the other, utilizing all training data from each set. This training process was monitored and analyzed as follows.

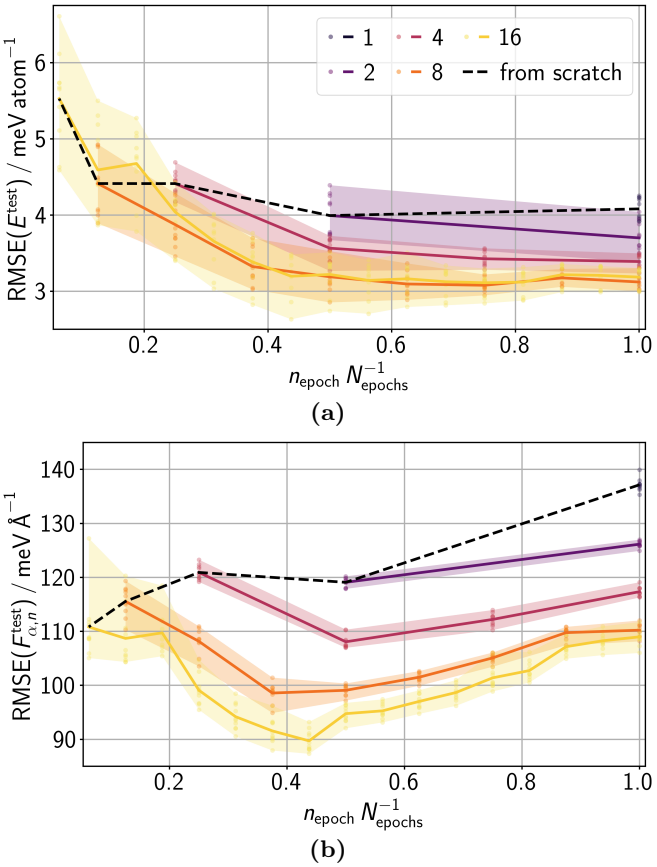

Figure 4: Test RMSEs of **(a)** energies E^{test} and **(b)** atomic force components $F_{\alpha,n}^{\mathrm{test}}$ after training 1 000 epochs on the (extended) data. Trainings were carried out on a sequence of 1, 2, 4, 8, and 16 data sets. A constant fraction of the training structures in the respective data set was utilized per epoch (scheme (1)). The total number of epochs N_{epochs} is higher for training in more sets, resembling the exploitation of previously acquired knowledge. In this figure and in Figures 5, 6, and 7, the underlying training data of each graph coincide at a given value of $n_{\mathrm{epoch}}\,N_{\mathrm{epochs}}^{-1}$. Dots represent RMSEs of individual HDNNP ensemble members, lines show their mean, and shaded areas span their range. The black dashed line represents the mean RMSE of training from scratch.

First, we show how much the continuation of lMLP training can improve the accuracy/cost ratio compared to starting the training after each data addition from scratch again. Therefore, we split the CRN data into $N_{\mathrm{data}} = \{1, 2, 4, 8, 16\}$ sets and trained each set for 1 000 epochs applying the lADS scheme (1) for the number of structures fitted per epoch (see Section 3.2). Hence, for a larger number of sets, the lMLP is trained in total for more epochs. This scenario resembles the frequently occurring case in which an MLP needs to be improved during a study and the previous MLP can be employed at no additional cost. Therefore, training for the same number of epochs with the same fraction of structures provides a comparison of learning from scratch and continual learning at equal effective cost. The accuracy of the test data after the initial training from scratch for each number of sets is highlighted in Figures 4 (a) and (b). The accuracy of continued training is consistently and significantly better than that of training from scratch for the same underlying training data. This trend highlights the benefit of continual learning compared to conventional iterative learning because it confirms that the previously learned expertise of the model can be exploited. The accuracy appears to converge to a lower limit for training in more sets.

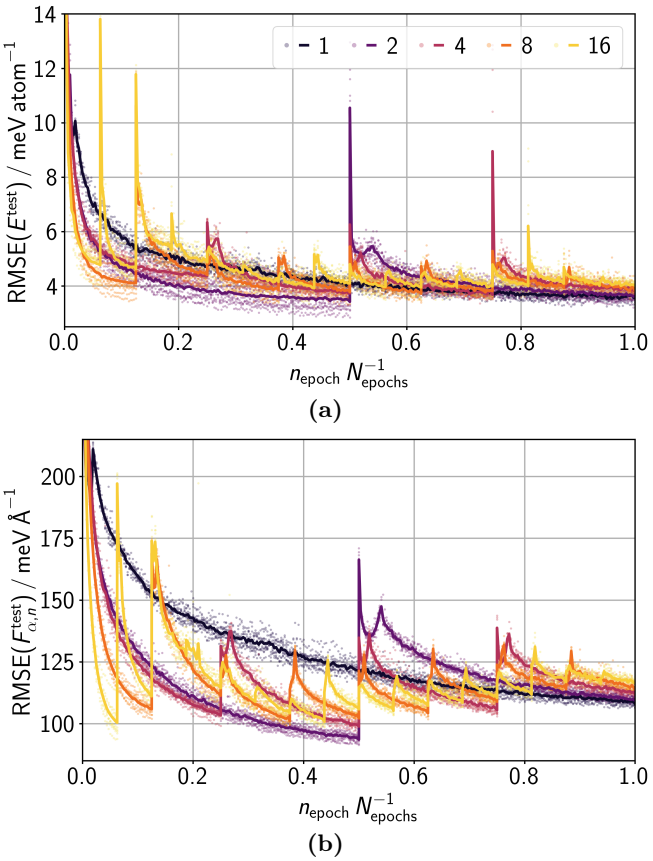

Figure 5: Test RMSEs of **(a)** energies E^{test} and **(b)** atomic force components $F_{\alpha,n}^{\mathrm{test}}$ for training the data in 1, 2, 4, 8, and 16 sets, with a constant number of fitted structures per epoch (scheme (2)). The total number of epochs $N_{\mathrm{epochs}} = 16\,000$ and hence structure evaluations were the same in all trainings.

The simplest learning case is training on all structures from the start, i.e., a stationary batch of data. However, this case is unfeasible in many applications that require either active learning or subsequent tasks with additional training data demands during the applications' progress. Hence, additional data sets or even a continuous stream of new data need to be learned after the initial training phase. Still, training on all data from the start can provide a reference for the maximally achievable accuracy of the lMLP, so that we can assess the quality of the results obtained with continual learning. Hence, we trained lMLPs on different numbers of data sets ($N_{\mathrm{data}} = \{1, 2, 4, 8, 16\}$) to go from this simplest learning case to more and more continual learning. To compare at the same absolute cost, the total number of structure evaluations in the training was the same for all cases. Figures 5 (a) and (b) show that the final test errors increase only slightly with more sets of data. Data addition is visible by spikes in the test RMSE, as the new test data can deviate significantly from previously trained data and can therefore lead to large errors. Recovery of accuracy in a small number of steps demonstrates good integration of the additional data. The peak height reduces with more data since the fraction of new data decreases and the probability increases that the necessary information has already been (partially) trained. Consequently, as expected, incremental learning does not yield the same accuracy as training on all data from the beginning. However, in many practical applications, the large cost reduction of continual learning is more important than the small error increase compared to iterative learning that starts for each data addition from scratch again.

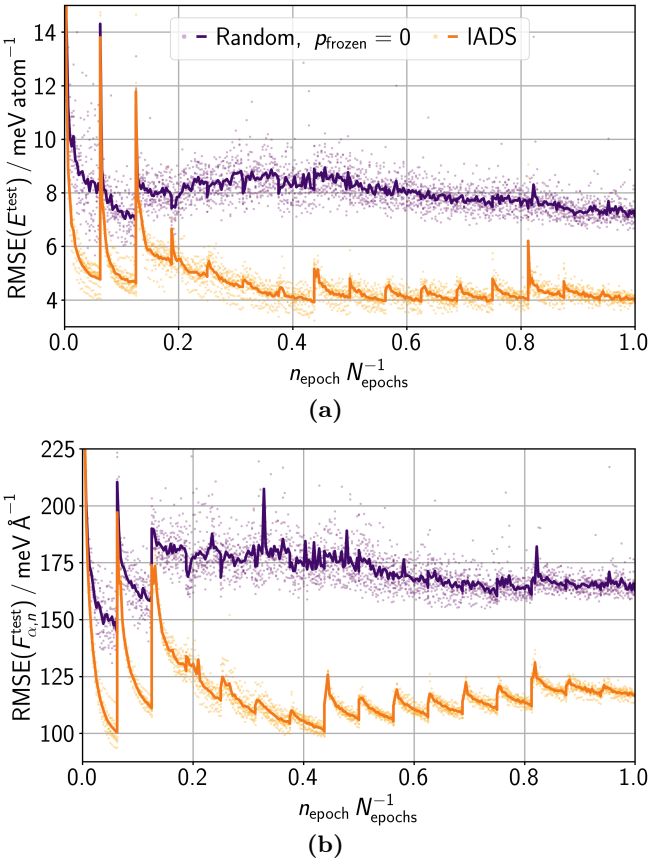

Figure 6: Test RMSEs of **(a)** energies E^{test} and **(b)** atomic force components $F_{\alpha,n}^{\mathrm{test}}$ for training the data in 16 sets according to scheme (2), with (I) random data selection and disabled stability–plasticity balance in the CoRe optimizer ($p_{\mathrm{frozen}} = 0$) and (II) lADS and $p_{\mathrm{frozen}} = 0.025$. Each set was trained for 1 000 epochs. Hence, both options, (I) and (II), required the same number of structure evaluations.

4.5. Lifelong Adaptive Data Selection

We now study the effect of lADS and the stability–plasticity balance of the CoRe optimizer on the learning process. The stability–plasticity balance adjusts the plasticity of the model weight parameters; that is, it can freeze important parameters to mitigate forgetting. In Figures 6 (a) and (b), we show how the two approaches change the training in 16 sets compared to the use of random data selection and disabled stability–plasticity balance ($p_{\mathrm{frozen}} = 0$). lADS and the stability–plasticity balance improve the final accuracy of the test energies and forces by 78% and 40%, respectively. We note that the number of training structure evaluations is the same (scheme (2)) so that the training costs are almost identical. For random data selection, the characteristic incremental learning convergence pattern vanishes after the initial training sets, since training is not focused on integrating the new data. Instead, the variance of the RMSEs of individual HDNNPs increases. In particular, large-error outliers occur more often, following no pattern. lADS yields a more predictable accuracy with an increase in RMSE after each data addition followed by rapid recovery. Despite this initial error increase, the accuracy is steadily better with lADS than with random data selection and disabled stability–plasticity balance.

lADS and the stability–plasticity balance of the CoRe optimizer can even improve accuracy if all data are trained from the start ($N_{\mathrm{data}} = 1$). The difference is less pronounced than in the continual learning case, but replacing random data selection with lADS and increasing p_{frozen} from 0 to 0.025 significantly reduces RMSE (E^{test}) from (4.8 ± 0.2) to (3.6 ± 0.2) meV atom^{-1} and RMSE $\left(F_{\alpha,n}^{\mathrm{test}}\right)$ from (120 ± 2) to (108 ± 2) meV Å^{-1}. The reasons for this effect are that the training is more focused on insufficiently represented training data and that the optimizer can balance the importance of model weight parameters. Consequently, we generally recommend the application of both features.

The best accuracy/cost ratio for training was observed when the number of fitted structures per epoch was ad-

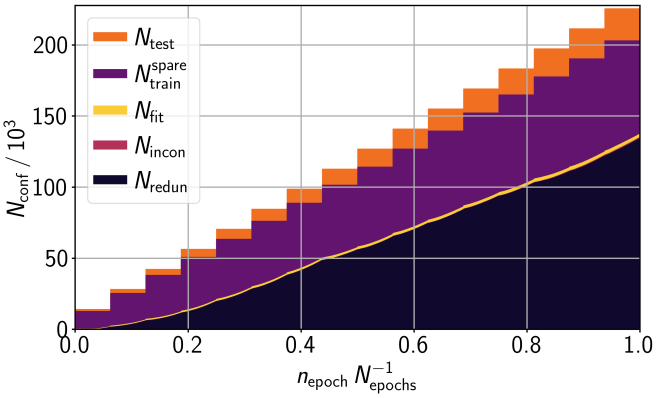

Figure 7: Total number of reference structure conformations N_{conf} as a function of the training progress $n_{\text{epoch}} N_{\text{epochs}}^{-1}$ (applying lADS scheme (3)). The colors represent the fractions of test data N_{test}, not employed $N_{\text{train}}^{\text{spare}}$ and employed training data N_{fit}, and training data disregarded due to inconsistencies N_{incon} and due to redundancy N_{redun}. Data assignment to the classes of being employed or not being employed in fitting can interchange in each epoch, while assignments to test or disregarded data are final.

justed based on a constant fraction of the training structures that were still employed for training (scheme (3)). This scheme is also important for a stable and well-balanced assignment of structures to be redundant in training. Figure 7 shows the evolution of the data assignments for training in 16 sets, whereby each set was trained for 1 000 epochs ($(26.7 \pm 0.2) \cdot 10^6$ force calculations in total). A steady increase of the number of structures sorted out can be observed. In each of the 10 individual HDNNP trainings, $134\,452 \pm 511$ or $(66.2 \pm 0.3)\%$ of the 202 986 training structures were assigned to be redundant in the end. Only 810 ± 43 or $(0.40 \pm 0.02)\%$ of the training structures were assigned to be inconsistent. Hence, the DFT data appear to be of good quality, and the lMLP is able to represent the majority of these data. Consequently, $67\,725 \pm 538$ or $(33.4 \pm 0.3)\%$ structures remain for rehearsal in further continued training. In this way, a significant speed-up can be provided compared to training again on all data for mitigating catastrophic forgetting. The reliability of the lADS approach is confirmed by the small variances in these assignments for the different individually trained HDNNPs of the ensemble.

Figures S1 (a) and (b) in the Supporting Information show that the accuracy for the test data after training each data addition remains at a similar level, despite that about two thirds of the training data have been removed. This trend confirms that training data classified as redundant is indeed not needed to retain previous expertise, since the latter is required to obtain low test errors. Moreover, due to the removal of training structures, fewer structures are fitted per epoch. With a decreasing number of added data, the training focuses on smaller data subsets, leading to fast data classifications. In this way, training becomes more efficient and continual learning of small amounts of additional data becomes reasonable. For training only on few additional data, the number of epochs per data addition can be reduced, since less information needs to be integrated. Due to Algorithm 3, these few new data points are still in the focus of training enabling efficient integration.

4.6. Lifelong Machine Learning Potentials for Exploration of Chemical Reaction Networks

Finally, the accuracy of an lMLP ensemble is analyzed in each training stage for previously trained and incoming data. Figures 8 (a) and (b) show the er-

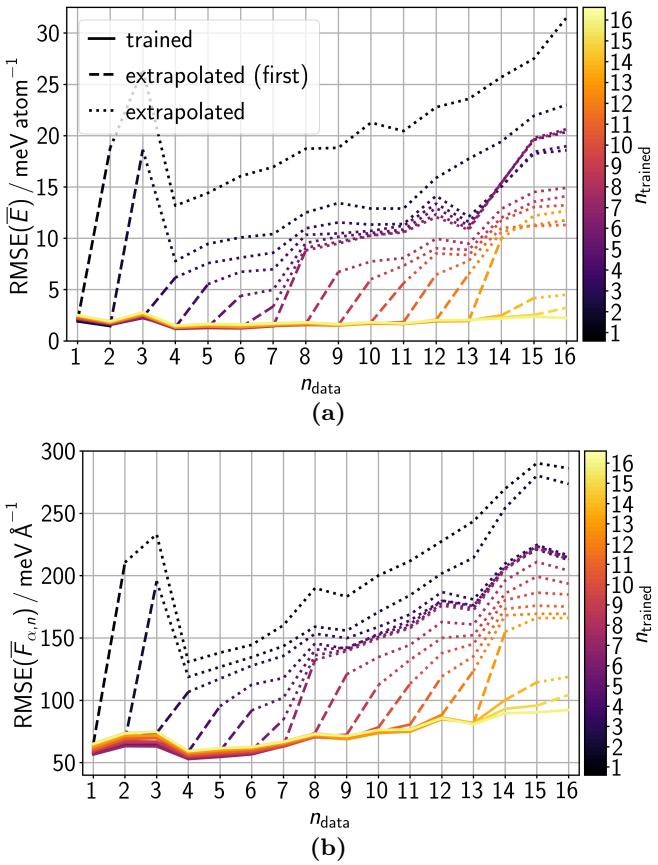

Figure 8: RMSEs of **(a)** energies $\overline{E}$ and **(b)** atomic force components $\overline{F}_{\alpha,n}$ evaluated for all data sets employing lMLP ensembles trained on different numbers of training data sets n_{trained} (applying lADS scheme (3)). Each training data set is a random subset of the respective data set, i.e., training data are contained in the RMSE evaluation. Lines are solid up to the last trained data set of the respective lMLP. The extrapolation to the data set to be trained next is shown as dashed line, while further extrapolations are connected by dotted lines.

rors for each number of trained data sets n_{trained} in our simulation of a rolling CRN exploration with data sets $n_{\text{data}} = \{1, ..., 16\}$. In general, the lMLP shows in every training stage very good accuracy for the data on which it was already trained. The energy accuracy is relatively constant for all trained data sets. The force RMSE increases slightly with increasing n_{data}. However, some variation is expected because the complexity of the training structures increases with n_{data} while the model architecture stays constant. Hence, the model could initially be too complex for the data and finally be affected by capacity issues.

We point out that the lMLP accuracy for the initial data remains almost constant with an increasing number of training stages. Only for the forces, a slight increase in error is notable. However, as the error also slightly increases for additionally trained data, the reason can be a capacity issue due to the constant model architecture. Consequently, the small subset of training data chosen by lADS is sufficient to retain previous expertise. Extrapolations to data to be trained result in higher errors, highlighting the efficiency of training. The more data sets are in between the last trained set and the evaluated set, the higher the error, since the ordering of the CRN data leads to an increasing difference in the data according to the progress of the chemical process. We note that the errors of the extrapolated predictions are still lower than the errors of the uMLP predictions (see Figure 3). Hence, the lMLP can efficiently and continuously learn additional data, while previous expertise is kept. Therefore, the lMLP approach is applicable for a rolling exploration. To produce efficient and accurate models, even when training is continued for a large number of additional data points, we expect algorithms to come into play that adjust (grow and shrink) the model architecture during training [116].

Finally, the accuracy needs to satisfy the requirements for CRN explorations (see Section 4.2). Figures 9 (a) and (b) reveal that the lMLP ensemble accuracy is below the target thresholds of 3.614 meV atom^{-1} and 100 meV Å^{-1}, different from the uMLPs investigated (Figures 3 (a) and (b)). In addition, Figures 9 (a) and (b) show the advantage of the Δ-learning approach. If an lMLP is trained in the same way on pure PBE data (lMLP_{PBE}), the resulting energy and force RMSEs will be approximately twice as large as those of the lMLP trained on PBE − GFN2 data. This reduction in error is required to yield chemical accuracy for is CRN data set.

We note that the element energy correction only marginally reduces the energy RMSE of the lMLP (Figure S2 in the Supporting Information), since training and performance evaluation are based on the same reference method (PBE/def2-TZVP(−GFN2)). Still, this result confirms that there is no systematic shift in the lMLP energies.

The results in Figures 9 (a) and (b) include the evaluation of training data (in contrast to Figures 3 to 6). For a fairer comparison with the uMLP results, pure test data need to be employed which are available for the individual HDNNPs of the lMLP ensemble. Table 2 shows

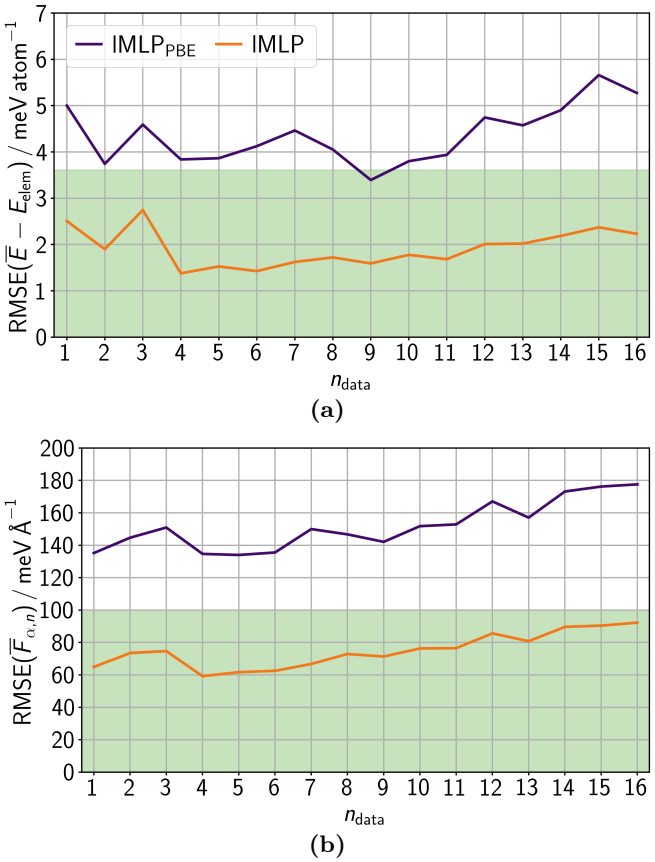

Figure 9: RMSEs of **(a)** energies $\overline{E}$ corrected by E_{elem} and **(b)** atomic force components $\overline{F}_{\alpha,n}$ evaluated for all data sets employing an lMLP ensemble trained on PBE energies (lMLP_{PBE}) and an lMLP ensemble trained on PBE − GFN2 energies (lMLP).

Table 2: Mean RMSEs of individual HDNNP ensemble members for final training data $E^{\text{train(final)}}$ and $F_{\alpha,n}^{\text{train(final)}}$, i.e., those data which are not disregarded in the last epoch, and test data E^{test} and $F_{\alpha,n}^{\text{test}}$. The given errors are the respective standard deviations. The RMSEs of the HDNNP ensemble are evaluated on all data $\overline{E}$ and $\overline{F}_{\alpha,n}$.

	RMSE
$E^{\text{train(final)}}$ / meV atom^{-1}	2.19 ± 0.04
E^{test} / meV atom^{-1}	3.29 ± 0.10
$\overline{E}$ / meV atom^{-1}	2.01
$F_{\alpha,n}^{\text{train(final)}}$ / meV Å^{-1}	121.1 ± 1.2
$F_{\alpha,n}^{\text{test}}$ / meV Å^{-1}	110.2 ± 0.9
$\overline{F}_{\alpha,n}$ / meV Å^{-1}	75.9

that the mean RMSE of the test energies also satisfies the chemical accuracy criterion. The mean RMSE of the test atomic force components is close to the target threshold. Since the ensemble results are, in general, better than the individual ensemble member predictions, the force RMSE is sufficiently small. We note that the RMSE of the final training data can be larger than the test RMSE because about two thirds of well represented training data were sorted out in the final epoch, while the test data were randomly chosen before training and remained unchanged.

5. CONCLUSIONS

In this work, we evaluated the applicability of universal machine learning potentials (uMLPs) and lifelong machine learning potentials (lMLPs) to drive the exploration of chemical reaction networks (CRNs). While the generalization capability of current uMLP parametrizations is not yet high enough for search trials in CRN explorations, lMLPs offer a promising alternative. An lMLP is a representation of the potential energy surface for arbitrary systems with uncertainty quantification that can be fine-tuned and extended in a rolling fashion. Hence, it unites accuracy, efficiency, and flexibility. In combination with a Δ-learning approach, our lMLP could reach chemical accuracy for the given $HCN + H_2O$ CRN data stream.

We proposed a modified lifelong adaptive data selection (lADS) algorithm to improve the continual learning performance of an lMLP. With this algorithm, an lMLP can handle conformation space extensions efficiently. The resulting accuracy is similar to that obtained by learning all data from the start, which is a much easier learning case but not feasible in applications with rolling data influx. The training data required to counteract forgetting can be reduced by lADS to a third in a reliable and stable way, while the accuracy of previous test data remains high. The latter is proven to be true even after adding data sets for the 15^{th} time, whereby each data set contained the same number of structures as the initial data set. Consequently, this evaluation of continual learning performance is significantly beyond our initial proof for one single addition of data [47]. Moreover, our results confirm that continual learning is able to take advantage of already acquired expertise to improve the final accuracy compared to training from scratch for the same number of epochs. Furthermore, we found that lADS and the continual learning features of the CoRe optimizer can improve the final accuracy not only in continual learning but also in learning stationary data.

Consequently, this work can be considered a proof of principle that lMLPs have all attributes to explore CRNs in a rolling fashion. Hence, lMLPs can be reliably applied on-the-fly during an exploration, where the CRN will be generated directly with an lMLP instead of DFT as in this work. Based on the uncertainty quantification (accessible in an MLP ensemble approach) it is then possible to decide on where additional DFT data needs to be generated for the refinement of the lMLP in subsequent lifelong learning epochs. To start such a process from a reasonable initial lMLP, the lMLP can be pre-trained on a large and diverse data set such as one of those employed for uMLPs. Naturally, the demand for such initial training events becomes rarer with increasing number of lMLP applications and, potentially, by community efforts to build generally applicable lMLPs (i.e., lMLPs that inherit universal features from diverse applications). Subsequently, continual learning can be applied to train on unknown structures occurring in the actual simulations of interest. In this way, the approach is similar to transfer learning or fine-tuning of foundation models on system-specific data, but continual learning harbors the advantage that learning can be continued for much more than one iteration.

DATA AVAILABILITY

The data underlying this study and related self-written software are openly available on Zenodo [117, 118].

CODE AVAILABILITY

The lMLP software will be made available on GitHub (`https://github.com/ReiherGroup/lMLP`) and PyPI (`https://pypi.org/project/lmlp`).

The SCINE Parrot software module will be made available on GitHub (`https://github.com/qcscine/parrot`) and PyPI (`https://pypi.org/project/scine-parrot`).

ACKNOWLEDGMENT

This work was supported by an ETH Zurich Postdoctoral Fellowship and by the NCCR Catalysis (grant number 180544), a National Centre of Competence in Research funded by the Swiss National Science Foundation.

[1] O. N. Temkin, A. V. Zeigarnik, and D. G. Bonchev, *Chemical Reaction Networks: A Graph-Theoretical Approach*, 1st ed. (CRC Press, 1996).

[2] M. Fialkowski, K. J. M. Bishop, V. A. Chubukov, C. J. Campbell, and B. A. Grzybowski, Architecture and evolution of organic chemistry, Angew. Chem. Int. Ed. **44**, 7263 (2005).

[3] S. Szymkuć, E. P. Gajewska, T. Klucznik, K. Molga, P. Dittwald, M. Startek, M. Bajczyk, and B. A. Grzybowski, Computer-assisted synthetic planning: The end of the beginning, Angew. Chem. Int. Ed. **55**, 5904 (2016).

[4] M. Feinberg, *Foundations of Chemical Reaction Network Theory*, Applied Mathematical Sciences (Springer, 2019).

[5] D. Rappoport, C. J. Galvin, D. Y. Zubarev, and A. Aspuru-Guzik, Complex chemical reaction networks from heuristics-aided quantum chemistry, J. Chem. Theory Comput. **10**, 897 (2014).

[6] Y. Kim, J. W. Kim, Z. Kim, and W. Y. Kim, Efficient prediction of reaction paths through molecular graph and reaction network analysis, Chem. Sci. **9**, 825 (2018).

[7] J. P. Unsleber and M. Reiher, The exploration of chemical reaction networks, Annu. Rev. Phys. Chem. **71**, 121 (2020).

[8] A. Baiardi, S. A. Grimmel, M. Steiner, P. L. Türtscher, J. P. Unsleber, T. Weymuth, and M. Reiher, Expansive quantum mechanical exploration of chemical reaction paths, Acc. Chem. Res. **55**, 35 (2022).

[9] M. Steiner and M. Reiher, Autonomous reaction network exploration in homogeneous and heterogeneous catalysis, Top. Catal. **65**, 6 (2022).

[10] I. Ismail, R. C. Majerus, and S. Habershon, Graph-driven reaction discovery: Progress, challenges, and future opportunities, J. Phys. Chem. A **126**, 7051 (2022).

[11] M. Wen, E. W. C. Spotte-Smith, S. M. Blau, M. J. McDermott, A. S. Krishnapriyan, and K. A. Persson, Chemical reaction networks and opportunities for machine learning, Nat. Comput. Sci. **3**, 12 (2023).

[12] J. T. Margraf, H. Jung, C. Scheurer, and K. Reuter, Exploring catalytic reaction networks with machine learning, Nat. Catal. **6**, 112 (2023).

[13] J. P. Unsleber, H. Liu, L. Talirz, T. Weymuth, M. Mörchen, A. Grofe, D. Wecker, C. J. Stein, A. Panyala, B. Peng, K. Kowalski, M. Troyer, and M. Reiher, High-throughput ab initio reaction mechanism exploration in the cloud with automated multi-reference validation, J. Chem. Phys. **158**, 084803 (2023).

[14] M. Woulfe and B. Savoie, Chemical networks from scratch with reaction prediction and kinetics-guided exploration, 10.26434/chemrxiv-2024-v15kp 10.26434/chemrxiv-2024-v15kp (2024).

[15] P. M. Zimmerman, Automated discovery of chemically reasonable elementary reaction steps, J. Comput. Chem. **34**, 1385 (2013).

[16] M. Bergeler, G. N. Simm, J. Proppe, and M. Reiher, Heuristics-guided exploration of reaction mechanisms, J. Chem. Theory Comput. **11**, 5712 (2015).

[17] S. Habershon, Sampling reactive pathways with random walks in chemical space: Applications to molecular dissociation and catalysis, J. Chem. Phys. **143**, 094106 (2015).

[18] W. M. C. Sameera, S. Maeda, and K. Morokuma, Computational catalysis using the artificial force induced reaction method, Acc. Chem. Res. **49**, 763 (2016).

[19] G. N. Simm and M. Reiher, Context-driven exploration of complex chemical reaction networks, J. Chem. Theory Comput. **13**, 6108 (2017).

[20] A. L. Dewyer, A. J. Argüelles, and P. M. Zimmerman, Methods for exploring reaction space in molecular systems, Wiley Interdiscip. Rev. Comput. Mol. Sci. **8**, e1354 (2018).

[21] G. N. Simm, A. C. Vaucher, and M. Reiher, Exploration of reaction pathways and chemical transformation networks, J. Phys. Chem. A **123**, 385 (2019).

[22] S. Maeda and Y. Harabuchi, Exploring paths of chemical transformations in molecular and periodic systems: An approach utilizing force, Wiley Interdiscip. Rev. Comput. Mol. Sci. **11**, e1538 (2021).

[23] J. P. Unsleber, S. A. Grimmel, and M. Reiher, Chemoton 2.0: Autonomous exploration of chemical reaction networks, J. Chem. Theory Comput. **18**, 5393 (2022).

[24] L.-P. Wang, A. Titov, R. McGibbon, F. Liu, V. S. Pande, and T. J. Martínez, Discovering chemistry with an ab initio nanoreactor, Nat. Chem. **6**, 1044 (2014).

[25] E. M.-N. nez, An automated method to find transition states using chemical dynamics simulations, J. Comput. Chem. **36**, 222 (2015).

[26] M. Döntgen, M.-D. Przybylski-Freund, L. C. Kröger, W. A. Kopp, A. E. Ismail, and K. Leonhard, Automated discovery of reaction pathways, rate constants, and transition states using reactive molecular dynamics simulations, J. Chem. Theory Comput. **11**, 2517 (2015).

[27] S. A. Vázquez, X. L. Otero, and E. Martinez-Nunez, A trajectory-based method to explore reaction mechanisms, Molecules **23**, 3156 (2018).

[28] J. Debnath, M. Invernizzi, and M. Parrinello, Enhanced sampling of transition states, J. Chem. Theory Comput. **15**, 2454 (2019).

[29] S. Grimme, Exploration of chemical compound, conformer, and reaction space with meta-dynamics simulations based on tight-binding quantum chemical calculations, J. Chem. Theory Comput. **15**, 2847 (2019).

[30] B. K. Shoichet, Virtual screening of chemical libraries, Nature **432**, 862 (2004).

[31] E. O. Pyzer-Knapp, C. Suh, R. Gómez-Bombarelli, J. Aguilera-Iparraguirre, and A. Aspuru-Guzik, What is high-throughput virtual screening? A perspective from organic materials discovery, Annu. Rev. Mater. Res. **45**, 195 (2015).

[32] A. S. Christensen, T. Kubař, Q. Cui, and M. Elstner, Semiempirical quantum mechanical methods for noncovalent interactions for chemical and biochemical applications, Chem. Rev. **116**, 5301 (2016).

[33] P. O. Dral, X. Wu, L. Spörkel, A. Koslowski, and W. Thiel, Semiempirical quantum-chemical orthogonalization-corrected methods: Benchmarks for ground-state properties, J. Chem. Theory Comput. **12**, 1097 (2016).

[34] J. Proppe, T. Husch, G. N. Simm, and M. Reiher, Uncertainty quantification for quantum chemical models of complex reaction networks, Faraday Discuss. **195**, 497 (2016).

[35] G. N. Simm and M. Reiher, Error-controlled exploration of chemical reaction networks with gaussian processes, J. Chem. Theory Comput. **14**, 5238 (2018).

[36] M. Bensberg and M. Reiher, Uncertainty-aware first-principles exploration of chemical reaction networks, J. Phys. Chem. A **128**, 4532 (2024).

[37] J. Behler, Perspective: Machine learning potentials for atomistic simulations, J. Chem. Phys. **145**, 170901 (2016).

[38] A. P. Bartók, S. De, C. Poelking, N. Bernstein, J. R. Kermode, G. Csányi, and M. Ceriotti, Machine learning unifies the modeling of materials and molecules, Sci.

Adv. **3**, e1701816 (2017).
[39] V. L. Deringer, M. A. Caro, and G. Csányi, Machine learning interatomic potentials as emerging tools for materials science, Adv. Mater. **31**, 1902765 (2019).
[40] F. Noé, A. Tkatchenko, K.-R. Müller, and C. Clementi, Machine learning for molecular simulation, Ann. Rev. Phys. Chem. **71**, 361 (2020).
[41] J. Westermayr, M. Gastegger, K. T. Schütt, and R. J. Maurer, Perspective on integrating machine learning into computational chemistry and materials science, J. Chem. Phys. **154**, 230903 (2021).
[42] S. Käser, L. I. Vazquez-Salazar, M. Meuwly, and K. Töpfer, Neural network potentials for chemistry: concepts, applications and prospects, Digital Discovery **2**, 28 (2023).
[43] Y. Yang, S. Zhang, K. D. Ranasinghe, O. Isayev, and A. E. Roitberg, Machine learning of reactive potentials, Annu. Rev. Phys. Chem. **75**, 371 (2024).
[44] C. Chen and S. P. Ong, A universal graph deep learning interatomic potential for the periodic table, Nat. Comput. Sci. **2**, 718 (2022).
[45] I. Batatia, P. Benner, Y. Chiang, A. M. Elena, D. P. Kovács, J. Riebesell, X. R. Advincula, M. Asta, W. J. Baldwin, N. Bernstein, A. Bhowmik, S. M. Blau, V. Cărare, J. P. Darby, S. De, F. D. Pia, V. L. Deringer, R. Elijošius, Z. El-Machachi, E. Fako, A. C. Ferrari, A. Genreith-Schriever, J. George, R. E. A. Goodall, C. P. Grey, S. Han, W. Handley, H. H. Heenen, K. Hermansson, C. Holm, J. Jaafar, S. Hofmann, K. S. Jakob, H. Jung, V. Kapil, A. D. Kaplan, N. Karimitari, N. Kroupa, J. Kullgren, M. C. Kuner, D. Kuryla, G. Liepuoniute, J. T. Margraf, I.-B. Magdău, A. Michaelides, J. H. Moore, A. A. Naik, S. P. Niblett, S. W. Norwood, N. O'Neill, C. Ortner, K. A. Persson, K. Reuter, A. S. Rosen, L. L. Schaaf, C. Schran, E. Sivonxay, T. K. Stenczel, V. Svahn, C. Sutton, C. van der Oord, E. Varga-Umbrich, T. Vegge, M. Vondrák, Y. Wang, W. C. Witt, F. Zills, and G. Csányi, A foundation model for atomistic materials chemistry, arXiv:2401.00096 [physics.chem-ph] 10.48550/arXiv.2401.00096 (2023).
[46] B. Focassio, L. P. M. Freitas, and G. R. Schleder, Performance assessment of universal machine learning interatomic potentials: Challenges and directions for materials' surfaces, ACS Appl. Mater. Interfaces (2024).
[47] M. Eckhoff and M. Reiher, Lifelong machine learning potentials, J. Chem. Theory Comput. **19**, 3509 (2023).
[48] Z. Chen and B. Liu, *Lifelong Machine Learning* (Morgan & Claypool Publishers, 2018).
[49] G. I. Parisi, R. Kemker, J. L. Part, C. Kanan, and S. Wermter, Continual lifelong learning with neural networks: A review, Neural Netw. **113**, 54 (2019).
[50] S. Grossberg, Adaptive resonance theory: How a brain learns to consciously attend, learn, and recognize a changing world, Neural Netw. **37**, 1 (2013).
[51] I. J. Goodfellow, M. Mirza, D. Xiao, A. Courville, and Y. Bengio, An empirical investigation of catastrophic forgetting in gradient-based neural networks, arXiv:1312.6211v3 [stat.ML] 10.48550/arXiv.1312.6211 (2015).
[52] D. Maltoni and V. Lomonaco, Continuous learning in single-incremental-task scenarios, Neural Netw. **116**, 56 (2019).
[53] R. Jinnouchi, J. Lahnsteiner, F. Karsai, G. Kresse, and M. Bokdam, Phase transitions of hybrid perovskites simulated by machine-learning force fields trained on the fly with Bayesian inference, Phys. Rev. Lett. **122**, 225701 (2019).
[54] R. Jinnouchi, F. Karsai, and G. Kresse, On-the-fly machine learning force field generation: Application to melting points, Phys. Rev. B **100**, 014105 (2019).
[55] M. Eckhoff and M. Reiher, Core optimizer: an all-in-one solution for machine learning, Mach. Learn.: Sci. Technol. **5**, 015018 (2024).
[56] J. Behler and M. Parrinello, Generalized neural-network representation of high-dimensional potential-energy surfaces, Phys. Rev. Lett. **98**, 146401 (2007).
[57] J. Behler, First principles neural network potentials for reactive simulations of large molecular and condensed systems, Angew. Chem. Int. Ed. **56**, 12828 (2017).
[58] J. Behler, Four generations of high-dimensional neural network potentials, Chem. Rev. **121**, 10037 (2021).
[59] J. Behler, Atom-centered symmetry functions for constructing high-dimensional neural network potentials, J. Chem. Phys. **134**, 074106 (2011).
[60] M. Gastegger, L. Schwiedrzik, M. Bittermann, F. Berzsenyi, and P. Marquetand, wACSF–weighted atom-centered symmetry functions as descriptors in machine learning potentials, J. Chem. Phys. **148**, 241709 (2018).
[61] T. W. Ko, J. A. Finkler, S. Goedecker, and J. Behler, A fourth-generation high-dimensional neural network potential with accurate electrostatics including non-local charge transfer, Nat. Commun. **12**, 398 (2021).
[62] A. A. Peterson, R. Christensen, and A. Khorshidi, Addressing uncertainty in atomistic machine learning, Phys. Chem. Chem. Phys. **19**, 10978 (2017).
[63] J. S. Smith, B. Nebgen, N. Lubbers, O. Isayev, and A. E. Roitberg, Less is more: Sampling chemical space with active learning, J. Chem. Phys. **148**, 241733 (2018).
[64] F. Musil, M. J. Willatt, M. A. Langovoy, and M. Ceriotti, Fast and accurate uncertainty estimation in chemical machine learning, J. Chem. Theory Comput. **15**, 906 (2019).
[65] G. Imbalzano, Y. Zhuang, V. Kapil, K. Rossi, E. A. Engel, F. Grasselli, and M. Ceriotti, Uncertainty estimation for molecular dynamics and sampling, J. Chem. Phys. **154**, 074102 (2021).
[66] D. P. Kingma and J. Ba, Adam: A method for stochastic optimization, in *3rd International Conference on Learning Representations (ICLR)* (San Diego, CA, USA, 2015).
[67] J. S. Smith, O. Isayev, and A. E. Roitberg, ANI-1: an extensible neural network potential with DFT accuracy at force field computational cost, Chem. Sci. **8**, 3192 (2017).
[68] C. Devereux, J. S. Smith, K. K. Huddleston, K. Barros, R. Zubatyuk, O. Isayev, and A. E. Roitberg, Extending the applicability of the ANI deep learning molecular potential to sulfur and halogens, J. Chem. Theory Comput. **16**, 4192 (2020).
[69] I. Batatia, D. P. Kovács, G. N. Simm, C. Ortner, and G. Csányi, MACE: Higher Order Equivariant Message Passing Neural Networks for Fast and Accurate Force Fields, in *Advances in Neural Information Processing Systems*, Vol. 35, edited by S. Koyejo, S. Mohamed, A. Agarwal, D. Belgrave, K. Cho, and A. Oh (Curran

Associates, Inc., 2022) pp. 11423–11436.
[70] A. Jain, G. Hautier, C. J. Moore, S. P. Ong, C. C. Fischer, T. Mueller, K. A. Persson, and G. Ceder, A high-throughput infrastructure for density functional theory calculations, Comput. Mater. Sci. **50**, 2295 (2011).
[71] A. Jain, S. P. Ong, G. Hautier, W. Chen, W. D. Richards, S. Dacek, S. Cholia, D. Gunter, D. Skinner, G. Ceder, and K. A. Persson, Commentary: The materials project: A materials genome approach to accelerating materials innovation, APL Mater. **1**, 011002 (2013).
[72] S. Zhang, M. Z. Makoś, R. B. Jadrich, E. Kraka, K. M. Barros, B. T. Nebgen, S. Tretiak, O. Isayev, N. Lubbers, R. A. Messerly, and J. S. Smith, Exploring the frontiers of chemistry with a general reactive machine learning potential, Nat. Chem. **16**, 727 (2024).
[73] D. M. Anstine, R. Zubatyuk, and O. Isayev, AIMNet2: A neural network potential to meet your neutral, charged, organic, and elemental-organic needs, 10.26434/chemrxiv-2023-296ch 10.26434/chemrxiv-2023-296ch (2024).
[74] S. Takamoto, S. Izumi, and J. Li, TeaNet: Universal neural network interatomic potential inspired by iterative electronic relaxations, Comput. Mater. Sci. **207**, 111280 (2022).
[75] S. Takamoto, C. Shinagawa, D. Motoki, K. Nakago, W. Li, I. Kurata, T. Watanabe, Y. Yayama, H. Iriguchi, Y. Asano, T. Onodera, T. Ishii, T. Kudo, H. Ono, R. Sawada, R. Ishitani, M. Ong, T. Yamaguchi, T. Kataoka, A. Hayashi, N. Charoenphakdee, and T. Ibuka, Towards universal neural network potential for material discovery applicable to arbitrary combination of 45 elements, Nat. Commun. **13**, 2991 (2022).
[76] S. Takamoto, D. Okanohara, Q.-J. Li, and J. Li, Towards universal neural network interatomic potential, J. Materiomics **9**, 447 (2023).
[77] K. Choudhary, B. DeCost, L. Major, K. Butler, J. Thiyagalingam, and F. Tavazza, Unified graph neural network force-field for the periodic table: solid state applications, Digital Discovery **2**, 346 (2023).
[78] A. Merchant, S. Batzner, S. S. Schoenholz, M. Aykol, G. Cheon, and E. D. Cubuk, Scaling deep learning for materials discovery, Nature **624**, 80 (2023).
[79] H. Yang, C. Hu, Y. Zhou, X. Liu, Y. Shi, J. Li, G. Li, Z. Chen, S. Chen, C. Zeni, M. Horton, R. Pinsler, A. Fowler, D. Zügner, T. Xie, J. Smith, L. Sun, Q. Wang, L. Kong, C. Liu, H. Hao, and Z. Lu, MatterSim: A deep learning atomistic model across elements, temperatures and pressures, arXiv:2405.04967 [cond-mat.mtrl-sci] 10.48550/arXiv.2405.04967 (2024).
[80] B. Deng, P. Zhong, K. Jun, J. Riebesell, K. Han, C. J. Bartel, and G. Ceder, CHGNet: Pretrained universal neural network potential for charge-informed atomistic modeling, Nat. Mach. Intell. **5**, 1031 (2023).
[81] H. Yu, M. Giantomassi, G. Materzanini, J. Wang, and G.-M. Rignanese, Systematic assessment of various universal machine-learning interatomic potentials, Mater. Genome Eng. Adv. **2**, e58 (2024).
[82] P. Zheng, R. Zubatyuk, W. Wu, O. Isayev, and P. O. Dral, Artificial intelligence-enhanced quantum chemical method with broad applicability, Nat. Commun. **12**, 7022 (2021).
[83] M. Schreiner, A. Bhowmik, T. Vegge, J. Busk, and O. Winther, Transition1x - a dataset for building generalizable reactive machine learning potentials, Sci. Data **9**, 779 (2022).
[84] J. Qi, T. W. Ko, B. C. Wood, T. A. Pham, and S. P. Ong, Robust training of machine learning interatomic potentials with dimensionality reduction and stratified sampling, npj Comput. Mater. **10**, 43 (2024).
[85] D. P. Kovács, J. H. Moore, N. J. Browning, I. Batatia, J. T. Horton, V. Kapil, W. C. Witt, I.-B. Magdău, D. J. Cole, and G. Csányi, MACE-OFF23: Transferable machine learning force fields for organic molecules, arXiv:2312.15211 [physics.chem-ph] 10.48550/arXiv.2312.15211 (2023).
[86] T. Weymuth, J. P. Unsleber, P. L. Türtscher, M. Steiner, J.-G. Sobez, C. H. Müller, M. Mörchen, V. Klasovita, S. A. Grimmel, M. Eckhoff, K.-S. Csizi, F. Bosia, M. Bensberg, and M. Reiher, Scine—software for chemical interaction networks, J. Chem. Phys. **160**, 222501 (2024).
[87] M. Bensberg, S. A. Grimmel, L. Lang, G. N. Simm, J.-G. Sobez, M. Steiner, P. L. Türtscher, J. P. Unsleber, T. Weymuth, and M. Reiher, qcscine/chemoton: Release 3.0.0, Zenodo 10.5281/zenodo.7928104 (2023).
[88] J.-G. Sobez and M. Reiher, Molassembler: Molecular graph construction, modification, and conformer generation for inorganic and organic molecules, J. Chem. Inf. Model. **60**, 3884 (2020).
[89] M. Bensberg, S. A. Grimmel, J.-G. Sobez, M. Steiner, J. P. Unsleber, and M. Reiher, qcscine/molassembler: Release 2.0.0, Zenodo 10.5281/zenodo.7928074 (2023).
[90] A. C. Vaucher and M. Reiher, Minimum energy paths and transition states by curve optimization, J. Chem. Theory Comput. **14**, 3091 (2018).
[91] M. Bensberg, C. Brunken, K.-S. Csizi, S. A. Grimmel, S. Gugler, J.-G. Sobez, M. Steiner, P. L. Türtscher, J. P. Unsleber, A. C. Vaucher, T. Weymuth, and M. Reiher, qcscine/readuct: Release 5.0.0, Zenodo 10.5281/zenodo.7928089 (2023).
[92] M. Bensberg, C. Brunken, K.-S. Csizi, S. A. Grimmel, S. Gugler, J.-G. Sobez, M. Steiner, P. L. Türtscher, J. P. Unsleber, T. Weymuth, and M. Reiher, qcscine/puffin: Release 1.2.0, Zenodo 10.5281/zenodo.7928099 (2023).
[93] M. Bensberg, S. A. Grimmel, J.-G. Sobez, M. Steiner, P. L. Türtscher, J. P. Unsleber, and M. Reiher, qcscine/database: Release 1.2.0, Zenodo 10.5281/zenodo.7928096 (2023).
[94] F. Neese, The ORCA program system, WIREs Comput. Mol. Sci. **2**, 73 (2012).
[95] F. Neese, Software update: The ORCA program system—version 5.0, WIREs Comput. Mol. Sci. **12**, e1606 (2022).
[96] J. P. Perdew, K. Burke, and M. Ernzerhof, Generalized gradient approximation made simple, Phys. Rev. Lett. **77**, 3865 (1996).
[97] F. Weigend and R. Ahlrichs, Balanced basis sets of split valence, triple zeta valence and quadruple zeta valence quality for H to Rn: Design and assessment of accuracy, Phys. Chem. Chem. Phys. **7**, 3297 (2005).
[98] J.-D. Chai and M. Head-Gordon, Systematic optimization of long-range corrected hybrid density functionals, J. Chem. Phys. **128**, 084106 (2008).
[99] V. A. Rassolov, M. A. Ratner, J. A. Pople, P. C. Redfern, and L. A. Curtiss, 6-31G* basis set for third-row atoms, J. Comput. Chem. **22**, 976 (2001).
[100] C. Bannwarth, E. Caldeweyher, S. Ehlert, A. Hansen, P. Pracht, J. Seibert, S. Spicher, and S. Grimme,

Extended tight-binding quantum chemistry methods, WIREs Comput. Mol. Sci. **11**, e1493 (2021).

[101] C. Bannwarth, S. Ehlert, and S. Grimme, GFN2-xTB—an accurate and broadly parametrized self-consistent tight-binding quantum chemical method with multipole electrostatics and density-dependent dispersion contributions, J. Chem. Theory Comput. **15**, 1652 (2019).

[102] X. Gao, F. Ramezanghorbani, O. Isayev, J. S. Smith, and A. E. Roitberg, TorchANI: A free and open source PyTorch-based deep learning implementation of the ANI neural network potentials, J. Chem. Inf. Model. **60**, 3408 (2020).

[103] C. R. Harris, K. J. Millman, S. J. van der Walt, R. Gommers, P. Virtanen, D. Cournapeau, E. Wieser, J. Taylor, S. Berg, N. J. Smith, R. Kern, M. Picus, S. Hoyer, M. H. van Kerkwijk, M. Brett, A. Haldane, J. Fernández del Río, M. Wiebe, P. Peterson, P. Gérard-Marchant, K. Sheppard, T. Reddy, W. Weckesser, H. Abbasi, C. Gohlke, and T. E. Oliphant, Array programming with NumPy, Nature **585**, 357 (2020).

[104] A. Paszke, S. Gross, F. Massa, A. Lerer, J. Bradbury, G. Chanan, T. Killeen, Z. Lin, N. Gimelshein, L. Antiga, A. Desmaison, A. Köpf, E. Yang, Z. DeVito, M. Raison, A. Tejani, S. Chilamkurthy, B. Steiner, L. Fang, J. Bai, and S. Chintala, PyTorch: An imperative style, high-performance deep learning library, in *33rd International Conference on Neural Information Processing Systems (NIPS)* (Vancouver, Canada, 2019) pp. 8026–8037.

[105] S. K. Lam, A. Pitrou, and S. Seibert, Numba: a LLVM-based Python JIT compiler, in *Second Workshop on the LLVM Compiler Infrastructure in HPC* (New York, NY, USA, 2015).

[106] R. T. Husistein, M. Reiher, and M. Eckhoff, NEAR: A training-free pre-estimator of machine learning model performance, arXiv:2408.08776 [cs.LG] 10.48550/arXiv.2408.08776 (2024).

[107] M. Eckhoff and M. Reiher, ReiherGroup/CoRe_optimizer: Release 1.1.0, Zenodo 10.5281/zenodo.11551858 (2024).

[108] J. P. Ferris and W. J. Hagan Jr., HCN and chemical evolution: The possible role of cyano compounds in prebiotic synthesis, Tetrahedron **40**, 1093 (1984).

[109] K. Ruiz-Mirazo, C. Briones, and A. de la Escosura, Prebiotic systems chemistry: New perspectives for the origins of life, Chem. Rev. **114**, 285 (2014).

[110] T. Das, S. Ghule, and K. Vanka, Insights into the origin of life: Did it begin from HCN and H_2O?, ACS Cent. Sci. **5**, 1532 (2019).

[111] P. E. Blöchl, Projector augmented-wave method, Phys. Rev. B **50**, 17953 (1994).

[112] A. Najibi and L. Goerigk, The nonlocal kernel in van der Waals density functionals as an additive correction: An extensive analysis with special emphasis on the B97M-V and ωB97M-V approaches, J. Chem. Theory Comput. **14**, 5725 (2018).

[113] S. Grimme, J. Antony, S. Ehrlich, and H. Krieg, A consistent and accurate ab initio parametrization of density functional dispersion correction (DFT-D) for the 94 elements H-Pu, J. Chem. Phys. **132**, 154104 (2010).

[114] S. Grimme, S. Ehrlich, and L. Goerigk, Effect of the damping function in dispersion corrected density functional theory, J. Comput. Chem. **32**, 1456 (2011).

[115] D. Rappoport and F. Furche, Property-optimized Gaussian basis sets for molecular response calculations, J. Chem. Phys. **133**, 134105 (2010).

[116] J. Yoon, E. Yang, J. Lee, and S. J. Hwang, Lifelong learning with dynamically expandable networks, in *6th International Conference on Learning Representations (ICLR)* (Vancouver, Canada, 2018).

[117] M. Eckhoff and M. Reiher, Lifelong and universal machine learning potentials for the exploration of chemical reaction networks – 1, Zenodo 10.5281/zenodo.14689930 (2025).

[118] M. Eckhoff and M. Reiher, Lifelong and universal machine learning potentials for the exploration of chemical reaction networks – 2, Zenodo 10.5281/zenodo.14689932 (2025).